Vertical Structure of Turbulence in the Lower Atmospheric Boundary Layer above a Deciduous Forest in Complex Terrain

Temple R. Lee,[a] Sandip Pal,[b] Tilden P. Meyers,[c] Praveena Krishnan,[a]
Rick D. Saylor,[a] and Mark Heuer[a,d]

[a] *NOAA/Air Resources Laboratory, Oak Ridge, Tennessee*
[b] *Atmospheric Science Group, Department of Geosciences, Texas Tech University, Lubbock, Texas*
[c] *NOAA/Air Resources Laboratory, Boulder, Colorado*
[d] *Oak Ridge Associated Universities, Oak Ridge, Tennessee*

Corresponding author: Dr. Temple R. Lee, temple.lee@noaa.gov

ABSTRACT

It is well known that parameterizations developed using observations from flat terrain have difficulty over complex terrain, which motivates a better understanding of turbulence exchanges occurring in these areas. In this work we addressed the question of how the vertical variability of turbulence features evolves over the lowest few hundred meters of the convective and nocturnal boundary layer above a forested ridge as a function of cloud cover and mean wind. We used one year of observations obtained from a WindCube V2.1 lidar installed in eastern Tennessee in the Southeast U.S. coupled with observations from a 60-m micrometeorological tower. The wind lidar has 20-m range gates spanning from 40 m to 300 m above ground. We used the lidar's high-frequency observations to derive turbulent kinetic energy (TKE), vertical velocity variance (σ_w^2), vertical velocity skewness (S), and kurtosis (K). We observed the largest decrease in the diurnal wind speed on clear, windy days. Under clear sky conditions, increasing TKE and σ_w^2 yielded positive S throughout the lower convective boundary layer. Under cloudy regimes, the distribution of TKE was height-independent and corresponded with smaller σ_w^2 and near-zero S. Our results provide insights into turbulence processes over forested complex terrain and support the refinement of turbulence parameterizations used in forecasting models.

1. Introduction

It has been well-established within the scientific community that the current approaches for representing turbulent exchange processes that were developed using observations from flat, homogenous terrain struggle in areas with complex terrain, diverse land cover types, or both (e.g., Wulfmeyer et al., 2011; Fernando et al., 2015). Despite much progress in mountain meteorology over the past few decades (Whiteman, 2000), large gaps remain in our knowledge of the multi-scale flow interactions occurring over complex terrain. Most of the research and forecast challenges arise because of somewhat limited observations over complex terrain, resulting in the weather phenomena in these areas remaining poorly understood. Furthermore, the proper characterizations of turbulent exchanges within these areas is an essential component for the surface-layer (SL) and atmospheric boundary layer (ABL) parameterization schemes forming the basis for numerical weather prediction (NWP) models. These models are critical for the prediction of a myriad of atmospheric phenomena that include wind gusts, cold air pools, convective- and orographically-induced clouds and precipitation, and other phenomena (e.g., Raupach and Finnigan, 1997; Adler et al., 2021).

Other studies have provided evidence of the impact of gentle topography on flow features through the use of observations and simulations (e.g., Finnigan and Belcher, 2004; Patton and Katul, 2009). However, the complexities in the kinematics within the ABL over mountainous regions, in particular near ridges and varying land cover types, pose challenges for the depiction of the aforementioned phenomena as well as for other applications. These applications include the monitoring and assimilating of trace gas mixing ratios into atmospheric transport models, the determination of regionally-representative measurements by exploiting both the local- and regional-scale variability of passive tracers and non-reactive aerosols, etc. (e.g., Lee et al., 2015, 2018; Pal et al., 2017).

Traditionally, SL exchange in NWP models have been represented using Monin-Obukhov Similarity Theory (MOST) (Monin and Obukhov, 1954), despite its well-documented limitations (e.g., Businger et al., 1971; Salesky and Chamecki, 2012; Sun et al., 2020). As both the horizontal and vertical resolution of NWP models continues to increase, and NWP models are better able to resolve increasingly fine-scale complexities in terrain and land cover, improved characterizations of turbulent processes over these areas becomes increasingly relevant. Studies of turbulent processes in regions of complex terrain allow the assessment of alternative MOST parameterizations, including the hockey-stick transition hypothesis (e.g., Sun et al., 2012; Van de Wiel et al., 2012; Grisogono et al., 2020; Lee et al., 2025) and SL parameterizations using Richardson-based scaling techniques (e.g., Dyer, 1974; Sorbjan and Grachev, 2010; Lee and Buban, 2020; Lee et al., 2021, 2023; Greene et al., 2022; Lee and Meyers, 2023). Additionally, ridgetop turbulence features are subjected to multi-scale flows and associated dynamical processes which include spatially-coherent turbulence structures, mountain wave and rotor-induced circulations, and synoptic-scale flows (Whiteman, 2000; De Wekker and Kossmann, 2015; Rotach et al., 2015; Wharton et al., 2017; Lehner and Rotach, 2018) which are oftentimes poorly represented in NWP models. Therefore, empirical insights into the spatial and temporal variability in turbulence over complex topography, obtained on a routine basis, remain sparse yet are crucial for improving parameterization schemes to resolve sub-grid processes of the coupled mountain-valley-plain atmosphere (e.g., Pal et al., 2016; Pal and Lee, 2019). Knowledge of turbulence characteristics within forests in complex terrain has routinely come from tower-based point observations at single or multiple heights (e.g., Baldocchi and Meyers, 1988a,b; Baldocchi and Meyers, 1989). Additionally lidar-derived high-resolution measurements have been used in recent decades to derive ABL turbulence characteristics (e.g., vertical velocity variance, σ_w^2, and skewness, S, of the vertical velocity) (e.g., Hogan et al., 2009). A focus of many previous studies has been to contrast turbulence characteristics under clear-sky days with turbulence characteristics on days with cloud-topped ABLs (e.g., Ansmann et al., 2010; Berg et al., 2017; Lareau et al., 2018; Dewani et al., 2023). When differentiating by cloud fraction, Lareau et al. (2018) found that ABL σ_w^2 was largest on days with cloud fractions between 0.3 and 0.5 but smallest on clear-sky days, whereas ABL S was smallest on days with cloud fractions exceeding 0.5 and largest on days with low cloud fractions. In contrast to the findings by Lareau et al. (2018), Dewani et al. (2023) found that the largest σ_w^2 typically occurred on clear-sky days and that σ_w^2 decreased as ABL moisture content increased.

The aforementioned studies relied upon traditional surface-based wind and aerosol lidars, which are well-suited for sampling the full ABL depth and characterizing turbulent mixing processes therein (e.g., Pal et al., 2010). However, wind and aerosol lidars, as well as other surface-based remote sensing instruments (e.g., atmospheric emitted radiance interferometers and microwave radiometers), are unable to sample within the lowest ~ 100 m of the ABL due to the partial overlap of the lidar transceiver system (e.g., Wagner et al., 2022). For this reason, other sampling approaches are required to provide better vertical sampling of turbulence near the land surface. Doing so is essential for advancing theories of turbulent exchange between the land surface and the atmosphere. Whereas sonic anemometers installed on micrometeorological towers are one approach to obtain information about near-surface turbulence characteristics, few towers are of sufficient height to fully resolve this vertical gap between the land surface and ~ 100 m above ground level (AGL). Recently, ground-based lidars have shown promise for deriving near-surface wind in addition to turbulence characteristics (e.g., Kumer et al., 2016; Wharton et al., 2017). Furthermore, by being merged with nearby turbulence observations obtained from micrometeorological towers, lidars can obtain details about the turbulence characteristics and structure within the lowest few hundred meters of the ABL over ridgetops (e.g., Wharton et al., 2017).

In this work, we used observations obtained from a wind lidar installed in eastern Tennessee in the Southeast U.S. coupled with observations from a nearby 60-m micrometeorological tower to examine:

1. how the vertical variability of turbulence features evolves above a low forested ridge as a function of cloud cover and as a function of different mean wind speeds in the lowest part of the convective boundary layer (CBL) and nocturnal boundary layer (NBL)

2. how turbulence features (i.e., turbulent kinetic energy, vertical velocity variance, skewness, and kurtosis) vary across subsets of meteorological conditions (i.e., different radiative and wind regimes)
3. differences in the impact of a well-mixed CBL versus a stratified NBL regime on ridgetop turbulence characteristics
4. the impact of different flow regimes (i.e., northeasterly versus southwesterly) on ridgetop turbulence characteristics.

2. Methods

2.1. Site description

We used observations obtained from Chestnut Ridge located in eastern Tennessee in the Southeast U.S. (Fig. 1a). A WindCube V2.1 wind lidar was installed at the location shown in Fig. 1b in May 2023 at 35.9618°N, 84.2865°W, 343 m above mean sea level (MSL) and has been in continuous operation since its installation. In this study, however, we focused on the first full year of measurements, i.e. those obtained between 1 June 2023 and 31 May 2024. Within a 5 km × 5 km area surrounding the site, the mean height of the topography is 274 ± 26 m. The ridge where the lidar is located is approximately 150 m above the surrounding valley and is one of several ridges that is located within the Tennessee Valley, which is oriented southeast to northeast. The Tennessee Valley is bounded by the Cumberland Mountains, which are about 1000 m MSL, to the north and west, and the Smoky Mountains (with an elevation up to ~ 2000 m MSL) to the south and east.

The wind lidar measurements were complemented by long-term observations from a 60-m micrometeorological tower also located along Chestnut Ridge (at 35.9311°N, 84.3323°W, 371 m MSL) approximately 5 km to the southwest of the lidar. The tower includes 30-min means of wind speed and direction; air temperature; relative humidity; pressure; incoming and outgoing photosynthetically active radiation; incoming and outgoing shortwave and longwave radiation; ground heat flux; and soil temperature and soil moisture. 30-min mean heat, water vapor, carbon dioxide fluxes, and turbulence statistics are computed from 10-Hz measurements. Most of the on-site measurements commenced in 2005 when the tower was installed, and details regarding the site and the on-site measurements are documented in previous studies (Wilson and Meyers, 2007, 2012, 2014; Lee et al., 2025). Incoming and outgoing shortwave and longwave radiation were obtained from a Kipp&Zonen CNR1 radiometer installed 36 m AGL, whereas a propeller anemometer installed at 43 m AGL was used to measure wind speed (WS) and wind direction (WD) at a

1-Hz sampling frequency and averaged to 30 minutes. Measurements from an RM Young 81000V three-dimensional sonic anemometer installed 43 m were used to obtain the u (horizontal), v (meridional), and w (vertical) wind components at 10 Hz. The measurements were used to calculate 30-min mean TKE and σ_w^2 and, along with the WS and WD measurements from the propeller anemometer, were compared against the lidar observations to provide confidence in the fidelity of the wind lidar measurements discussed in Section 2.2.

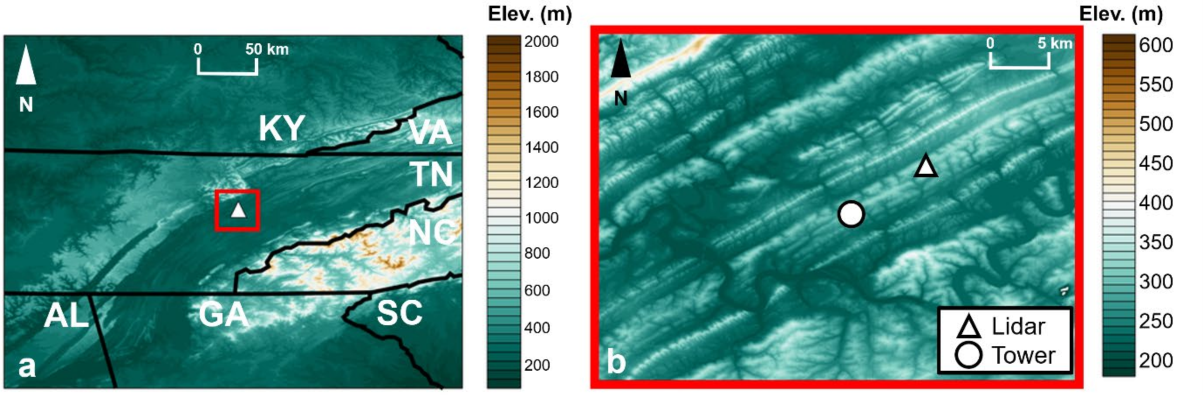

Fig. 1. (a) The location of the study site (white triangle). The red box in panel (a) denotes the location of the map in panel (b). The white triangle and white circle in panel (b) indicates the location of the lidar and micrometeorological tower, respectively.

2.2. Wind Lidar Derived Turbulence Quantities

The WindCube V2.1 has a pulsed Doppler heterodyne laser and uses 20-m range gates spanning from 40 to 300 m AGL for a total of 14 range gates, which is comparable to the dynamic range that has been used in previous studies to examine turbulence characteristics and structures within the lower ABL (e.g., Wharton et al., 2017; Liao et al., 2020). The lidar's lowest range gate is located at approximately 1.5 times the adjacent canopy height (h_c), which was estimated to be around 25 ± 3 m in previous work (Wilson et al., 2012; Lee et al., 2025). The lidar has a 1-Hz sampling rate and a manufacturer-stated radial wind speed range of -23 m s^{-1} to +23 m s^{-1}, wind speed accuracy of 0.1 m s^{-1}, and wind direction accuracy of 2°. The manufacturer-stated speed uncertainty is 1.4–2.6% between 40 and 80 m, 0.6–1.4% between 80 and 120 m, and 0.6–0.8% between 120 and 135 m.

The Doppler beam swinging (DBS) technique (e.g., Strauch et al., 1984; Wharton et al., 2017; Robey and Lundquist, 2022) is used to obtain wind and turbulence characteristics over the lowest 300 m of the atmosphere. Five scans are used within the DBS technique, whereby four beams are emitted 28° off-zenith in each of the four cardinal wind directions (i.e., north, east, south, and west), and a fifth beam is emitted in the vertical direction (i.e., 0° zenith angle). To ensure a high-quality dataset from the wind lidar, we removed values when the carrier-to-noise ratio (CNR) was less than -23 following previous work (e.g., Wharton et al., 2017). We used the 1-Hz observations obtained from the lidar to calculate select turbulence statistics, i.e., σ_w^2, TKE, S, and K, on 30-min timesteps. TKE was computed using the high-frequency measurements of the u, v, and w wind components derived from the lidar using the following equation after rotating the wind components into the standard meteorological convention whereby $u > 0$ m s^{-1} and $v > 0$ m s^{-1} indicate southerly and westerly winds, respectively, and $w > 0$ m s^{-1} indicates upward vertical velocities. Upon introducing these corrections, we computed TKE as

$$TKE = 0.5(\sigma_u^2 + \sigma_v^2 + \sigma_w^2) \qquad (1)$$

In the above equation, σ_u^2, σ_v^2, and σ_w^2 are the variances in the u-, v-, and w- wind components, respectively. The skewness (S) and kurtosis (K) were computed as a function of the vertical w perturbation (w') and the standard deviation in the vertical wind velocity (σ_w):

$$S = \left(\frac{\overline{w'^3}}{\overline{w'^2}}\right)^{3/2} \qquad (2)$$

$$K = \left(\frac{\overline{w'}}{\sigma_w}\right)^{4} \qquad (3)$$

The quantity S represents the degree of symmetry / asymmetry in the w distribution. Physically, S is interpreted as the vertical transport of $\overline{w'^2}$; thus positive (negative) S indicates an upward (downward) transport of TKE and $\overline{w'^2}$ (e.g., Hogan et al., 2009). The K profiles are used as an indicator of turbulence intermittency and degree of mixing at different sampling heights (e.g., Pal et al., 2010; McNicholas and Turner, 2014).

As discussed in Wharton et al. (2017), the turbulence quantities derived from the wind lidar represent a volume-averaged scan because of the divergence in the lidar beam in the zenith direction, rather than a point turbulence measurement that would be derived using a sonic anemometer. Furthermore, cross-contamination in the wind components can occur, affecting σ_u^2, σ_v^2, and σ_w^2 (e.g., Sathe and Mann, 2013; Newman et al., 2016; Wharton et al., 2017) and thus further motivating the need for comparison against turbulence observations derived from a micrometeorological tower which we do in Section 3.1.

After calculating TKE, σ_w^2, S, and K, we performed additional filtering of these datasets by removing physically-unrealistic values, i.e. TKE > 10 m^2 s^{-2} and σ_w^2 > 5 m^2 s^{-2}, following the procedure outlined in Lee et al. (2023). The percent data completion for TKE, σ_w^2, S, and K exceeded 90%, as shown in Appendix A, but decreased as a function of height due to clouds and fog. Consequently, the highest lidar range gate, i.e. at 300 m AGL, had a percent data completion of 52% for TKE and ~ 70% for σ_w^2, S, and K.

2.3. Classification of Meteorological Regimes

2.3.1. Daytime Radiative and Wind Regimes

To distinguish among different meteorological regimes at the study site during the daytime, we used the 30-min mean observations of shortwave radiation obtained from the 60-m micrometeorological tower near the lidar. The shortwave radiation observations enabled us to classify different radiative regimes. We identified different radiative regimes by computing the clearness index (Fig. 2a). As described and implemented in previous work to help classify different meteorological regimes (e.g., Pal et al., 2014; Lee et al., 2024) the C_{index}, is calculated as

$$C_{index} = \frac{\sum SW_o}{\sum SW_t} \tag{4}$$

In the above equation, $\sum SW_o$ is the daily total sum of incoming shortwave radiation (SW_{in}) which we measured using the Kipp&Zonen CNR1 radiometer installed the Chestnut Ridge tower. $\sum SW_t$, computed following the procedure described in Whiteman and Allwine (1986), is the sum of the total theoretical maximum incoming solar radiation that could be received on a given day and varies as a function of latitude, longitude, and both by time of day and day of year (e.g., Whiteman and Allwine, 1986; Whiteman et al., 1999).

We distinguished among different WS regimes by computing the mean daytime (i.e., SW_{in} > 0 W m$^{-2,}$ typically spanning from about 0750 LST to 1730 LST in the winter to about 620 LST to 2100 LST in the summer) wind speed (i.e., $\overline{WS_{day}}$) from the RM Young propeller at the micrometeorological tower. The $\overline{WS_{day}}$ ranged from 0.06 m s^{-1} to 7.2 m s^{-1} during the one-year study period and had a median of 2.13 m s^{-1} (Fig. 2b).

After computing the C_{index} and $\overline{WS_{day}}$, we used the percentiles shown in Fig. 2a and Fig. 2b to distinguish among four distinct meteorological conditions. Clear (cloudy) days were identified as those with C_{index} > 66th percentile (C_{index} < 33rd percentile), and days with weak (strong) winds as those with $\overline{WS_{day}}$ < 33rd percentile ($\overline{WS_{day}}$ > 66th percentile). Sensitivity tests, shown in Appendix B, indicated that our conclusions were unaffected by our choice of percentile. The four different meteorological regimes were as follows, with the number of days (N) within each these classifications is shown in parentheses:

I. Clear and weak winds: C_{index} > 66th percentile, $\overline{WS_{day}}$ < 33rd percentile (N = 49 days)

II. Clear and strong winds: C_{index} > 66th percentile, $\overline{WS_{day}}$ > 66th percentile (N = 37 days)

III. Cloudy and weak winds: C_{index} < 33rd percentile, $\overline{WS_{day}}$ < 33rd percentile (N = 37 days)

IV. Cloudy and strong winds: C_{index} < 33rd percentile, $\overline{WS_{day}}$ > 66th percentile (N = 38 days)

After distinguishing among these meteorological regimes, we computed composites of the mean cycles during the daytime only which we defined as between 0700 LST and 1900 LST for each sampling height. When determining the WD means, we first converted each observed WD into its u and v components, determined the mean u and v, and computed WD using these means.

We further investigated wind and turbulence characteristics within each of the four aforementioned regimes by determining the w frequency distribution and, to further place our results into the context of previous studies, by computing the mean profiles of the wind and turbulence quantities.

2.3.2. Nighttime Radiative and Wind Regimes

To distinguish among different meteorological regimes at the study site during the nighttime, we again used radiation observations from the 60-m micrometeorological tower. In this instance, we utilized the longwave radiation observations under the premise that more negative values of net radiation (R_{net}) during the nighttime correspond to clear skies due to emitted longwave radiation. We defined nighttime hours as those between 0000 and 0400 LST to ensure our results were unaffected by processes occurring during the early-morning or early evening transition periods around sunrise and sunset, respectively. Across all days in the study period, the median nighttime R_{net} was -60 W m^{-2} (Fig. 2c). The median nighttime wind speed (i.e., $\overline{WS_{night}}$) was 2.9 m s^{-1} and ranged from 0.2 m s^{-1} to 9.8 m s^{-1} (Fig. 2d). Similar to the daytime meteorological conditions, we distinguished among four different regimes during the nighttime which we defined as follows and that are distributed throughout the year. As in Section 2.3.1., the number of days within each these classifications is shown in parentheses:

I. Clear and weak winds: R_{net} < 33rd percentile, $\overline{WS_{night}}$ < 33rd percentile (N = 33 days)

II. Clear and strong winds: R_{net} < 33rd percentile, $\overline{WS_{night}}$ > 66th percentile (N = 34 days

III. Cloudy and weak winds: R_{net} > 66th percentile, $\overline{WS_{night}}$ < 33rd percentile (N = 38 days)

IV. Cloudy and strong winds: R_{net} > 66th percentile, $\overline{WS_{night}}$ > 66th percentile (N = 34 days)

As with the different classifications of daytime radiative and wind regimes, we found that our conclusions for the nighttime regimes were largely unaffected by our choice of percentile. This conclusion was based upon sensitivity tests conducted (not shown) across different percentiles. As we did for the daytime cases, to further place our results into the context of previous studies, we determined the w frequency distributions during these different regimes and $\overline{WS}$, $\overline{WD}$, $\overline{TKE}$, $\overline{\sigma_w^2}$, $\bar{S}$, and $\bar{K}$ vertical profiles between 0000 and 0400 LST.

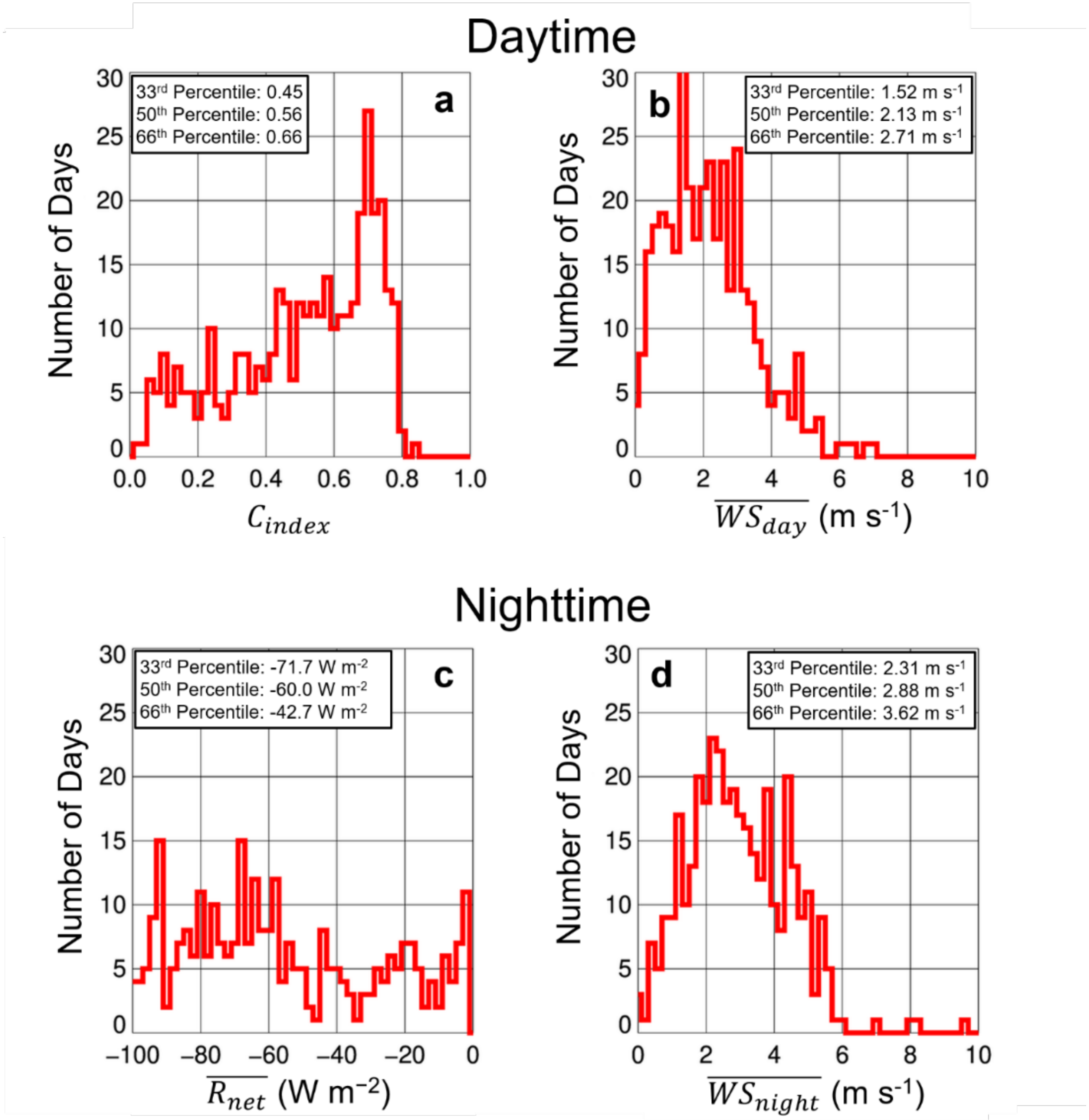

Fig. 2. Histogram of the daytime (i.e., SW_{in} > 0 W m^{-2}) (a) C_{index} and (b) $\overline{WS_{day}}$, also when SW_{in} > 0 W m^{-2}. A binsize of 0.02 and 0.2 m s^{-1} is used in panels (a) and (b), respectively. Panels (c) and (d) show the histogram of $\overline{R_{net}}$ during the nighttime (i.e., 0000–0400 LST) and $\overline{WS_{night}}$. A binsize of 2 W m^{-2} and 0.2 m s^{-1} is used in panels (c) and (d), respectively. As for panels (a) and (b), the 33rd, 50th, and 66th percentiles are shown in the upper portion of panels (c) and (d).

2.3.3. Wind Direction Regimes

To fulfill the fourth objective of this work enumerated in Section 1, we evaluated how turbulence characteristics varied as a function of WD by selecting days with near-constant WD. To this end, we classified a day as having constant WD if at least 90% of the 30-min observations on the given day were from the same direction (i.e., northeast, southeast, southwest, or northwest, which we defined as 0° ≤ WD < 90°, 90° ≤ WD < 180°, 180° ≤ WD < 270°, and 270° ≤ WD < 360°, respectively). During the one-year study period, based on this selection criteria, 25 days had constant northeasterly winds, and 45 days had constant southwesterly winds. Three of the days had constant northwesterly winds, whereas southeasterly winds were not observed for at least 90% of the 30-min observations on any day during the study period. Because of the small number of cases with northwesterly winds, we restricted our analyses to days only with constant northeasterly winds and days with constant southwesterly winds.

3. Results

3.1. Intercomparison between Lidar- and Tower-Derived Wind and Turbulence Observations

3.1.1. Wind Speed and Wind Direction Intercomparison

To help provide us with confidence in the fidelity of the observations from the wind lidar, we used wind roses to compare the wind speeds and wind directions obtained from the propeller anemometer installed on the micrometeorological tower at Chestnut Ridge with the observations from the wind lidar. The morning (i.e., 0800–1200 LST) and nighttime (i.e., 0000–0400 LST) measurements from the tower's above-canopy measurements and from the lidar's lowest range gate (i.e., 40 m AGL) exhibited a bimodal distribution yielding dominant southwesterly and northeasterly winds which is consistent with previous work from the study region (e.g., Lee et al., 2025). During both the morning and nighttime, southwesterly winds and northeasterly winds were nearly equally prevalent at the micrometeorological tower (Fig. 3a, Fig. 3c). When assessing the seasonal variability in the wind speeds, we found that the warm season had slightly weaker mean winds and a larger percentage of daytime southwesterly flows than during the cool season (not shown).

Examination of the wind speeds and wind directions obtained from the wind lidar indicated that, although the lidar-retrieved winds at 40 m AGL exhibited a bimodal distribution, there was a stronger westerly and east-northeasterly wind component at this height (Fig. 3d, Fig. 3f). During the afternoon (i.e., 1200–1600 LST), easterly winds were less frequent at the tower than at the lidar's lowest range gate, with southwesterly and westerly winds being much more dominant (Fig. 3b, Fig. 3d). The period from 0800–1200 LST is the period when the site experiences morning transition and a growing CBL regime and associated changes in both horizontal wind speed and direction take place on regular basis. For instance, as will be shown in Section 3.2, this is the period associated with a winds speed decrease (i.e., a shift from the NBL to the CBL) and changes from a stratified NBL to a well-mixed CBL regime (i.e., diverse wind directions to similar wind direction at all levels). Consequently, higher discrepancies between lidar and tower observations were also observed during this transition period (e.g., the tower showing the presence of more southwesterly to northeasterly components whereas the lidar showed more easterly and westerly components (cf. Fig. 3a). Overall, there was good agreement between the lidar-derived and tower-derived WS, but the lidar underestimates WS compared with those from the tower, particularly for higher WS (Fig. 4). As a result, the R^2 for the relationship between these quantities, of 0.65, was lower than studies that have been conducted at sites in flat terrain, whereby R^2 was found to be ~ 1 (e.g., Knoop et al., 2021).

When evaluating the wind roses for the lidar's upper sampling heights (here, 200 m AGL and 300 m AGL), we found that, irrespective of time of day, southwesterly winds were more common than winds with an easterly component. These southwesterly winds occurred more frequently at 300 m AGL than at 200 m AGL (Fig. 3g – 3l). Overall, the differences in the wind direction that we find between the micrometeorological tower and wind lidar highlight that, even though the two sampling locations are located only about 5 km apart along the same mountain ridge, finescale differences in local topography surrounding the two sites may be responsible for the observed differences in wind speed and wind direction.

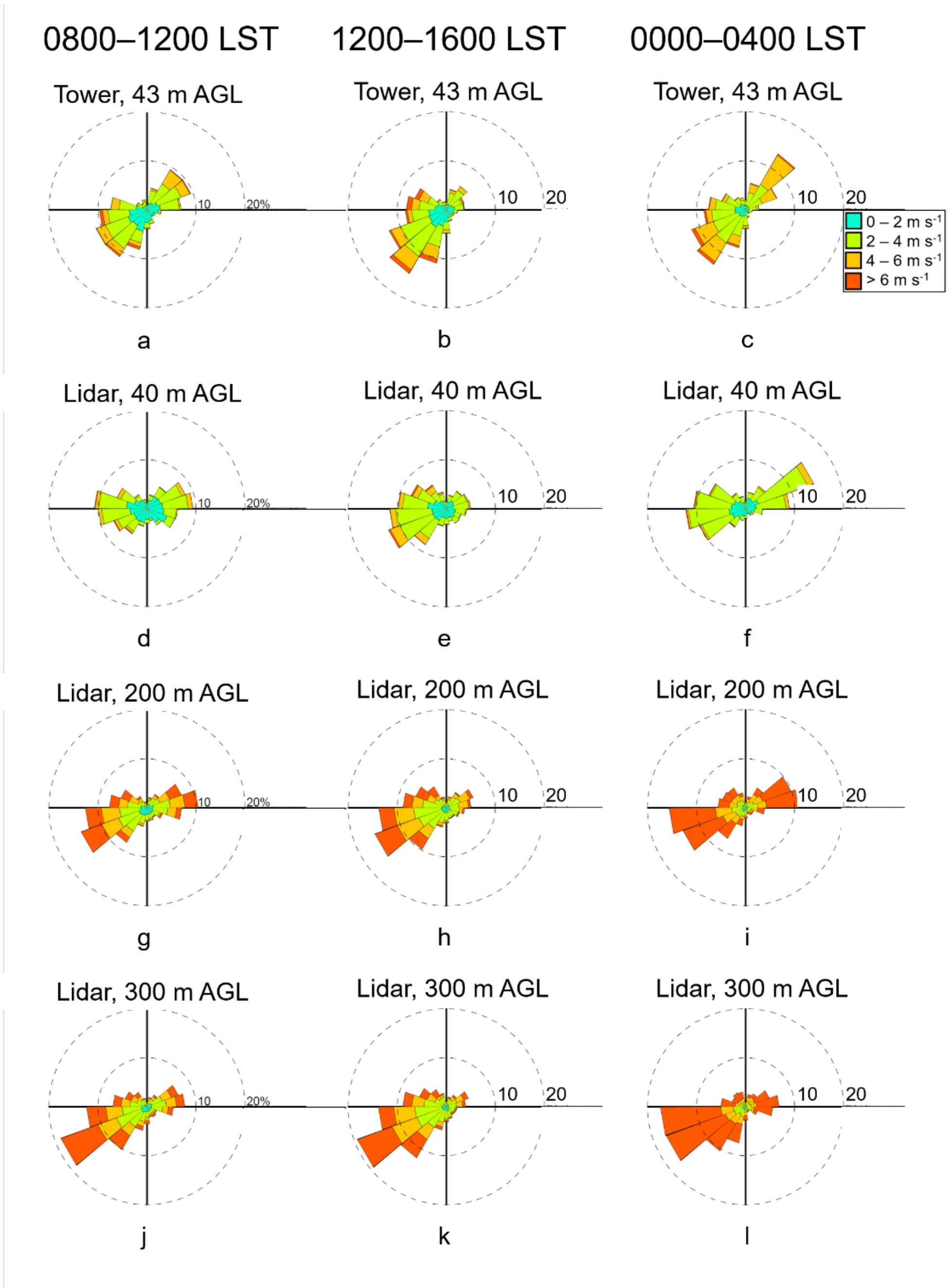

Fig. 3. (a) The wind rose for winds measured 43 m AGL at the 60-m micrometeorological tower between 0800 and 1200 LST. Same for (b) and (c) but for winds sampled between 1200 and 1600 LST and between 0000 and 0400 LST, respectively. Panels (d) – (f) show winds sampled 40 m AGL from the wind lidar between 0800 and 1200 LST, 1200 and 1600 LST and between 0000 and 0400 LST, respectively. Same for panels (g) – (i) and panels (j) – (l), but for 200 m AGL and 300 m AGL, respectively. A bin size of 20° is used in all panels. Turquoise, light green, orange, and red correspond with winds < 2 m s^{-1}, 2–4 m s^{-1}, 4–6 m s^{-1}, and > 6 m s^{-1}, respectively. Note that the spatial separation between the micrometeorological tower and the wind lidar is about 5 km.

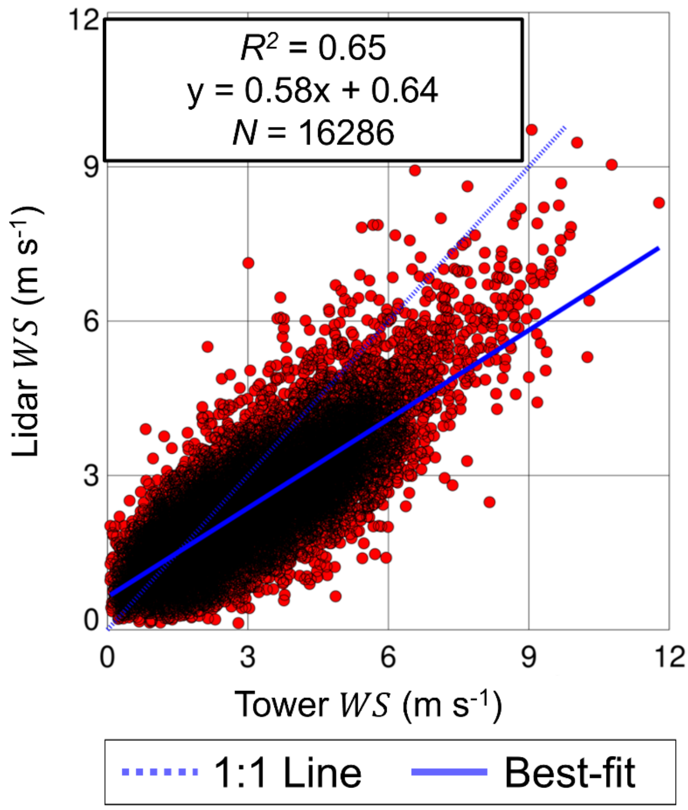

Fig. 4. The relationship between the lidar-derived WS (at 40 m AGL) and tower-derived WS (at 43 m AGL). The R^2 the best-fit equation (where *y* and *x* correspond with the lidar values and tower values, respectively), and N are shown in a box at the upper right. The dotted and solid blue lines indicate unity and the line of best fit, respectively.

3.1.2. Turbulence Intercomparison

To obtain additional confidence in the measurements from the wind lidar, we evaluated the relationship between the σ_w^2 and TKE obtained from the sonic anemometer installed on the micrometeorological tower and σ_w^2 and TKE derived from the lowest range gate of the wind lidar using an orthogonal (i.e., Deming) regression. We found that the slope of the line of best fit (m_b) between lidar-derived and tower-derived quantities during the afternoon (i.e., 1200–1600 LST, where LST = UTC – 5) for σ_w^2 and TKE was 0.40 and 0.41, respectively (Fig. 5a, Fig. 5b). During the nighttime (i.e., 0000–0400 LST) m_b between lidar-derived and tower-derived σ_w^2 (TKE) was lower than during the afternoon as m_b was 0.33 (0.37) (Fig. 5c, Fig. 5d). Furthermore, R^2 was lower during the nighttime than during the afternoon for both σ_w^2 and TKE. Analogous results (not shown) were found when conducting these evaluations as a function of different wind direction regimes to distinguish between times when the wind lidar was upwind (downwind) from the micrometeorological tower which correspond with northeasterly (southwesterly) winds. Furthermore, there was no clear relationship between the magnitude of observed differences in the tower- and lidar-derived turbulence characteristics and observed temperature at the micrometeorological tower (cf. Fig. 5).

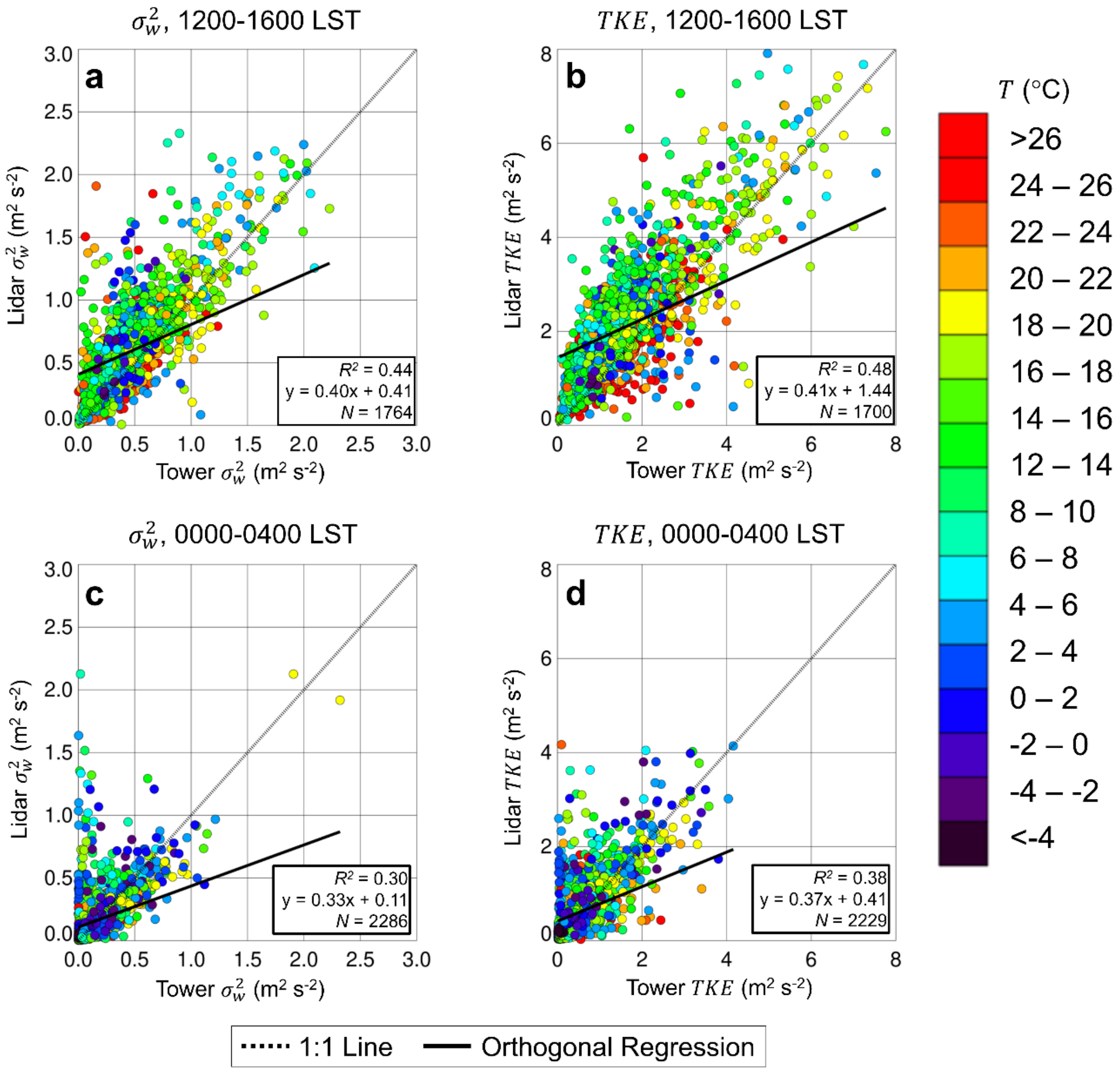

Fig. 5. (a) Wind lidar σ_w^2 versus the micrometeorological tower σ_w^2 and (b) lidar TKE versus the micrometeorological tower TKE between 1 June 2023 and 31 May 2024 between 1200 and 1600 LST. Same for panels (c) and (d), but for 1200–1600 LST and 0000–0400 LST, respectively. The dotted and solid black lines indicate unity and the line of best fit computed using orthogonal regression, respectively. The R^2 the best-fit equation, computed using an orthogonal regression (where y and x correspond with the lidar-derived and tower-derived values, respectively), and N are shown in a box on the lower right of each subpanel. Each point is color-coded by air temperature (T, see legend to the right of the figure). Note that the tower-derived TKE and σ_w^2 were sampled at 43 m AGL, whereas the lidar-derived TKE and σ_w^2 were sampled at 40 m AGL.

3.1.3. Power Spectra

To further enhance our confidence in the fidelity in the lidar's observations and in the turbulence quantities derived from it, we computed the vertical velocity power spectra for select sampling heights (i.e., 40 m AGL, 100 m AGL, and 200 m AGL) following for example Brugger et al. (2016). As shown in Fig. 6, the slope at the different sampling heights is comparable with the theoretical slope of the inertial subrange (i.e., $f^{-2/3}$). Furthermore, there exists height dependence to the maximum in the power spectrum, which occurs at the lowest sampling frequencies and is consistent with findings that have been reported within previous studies that have been conducted over flat terrain including for example northwestern Minnesota (Kaimal et al., 1976) and Germany's Lower Rhine region (Maurer et al., 2016).

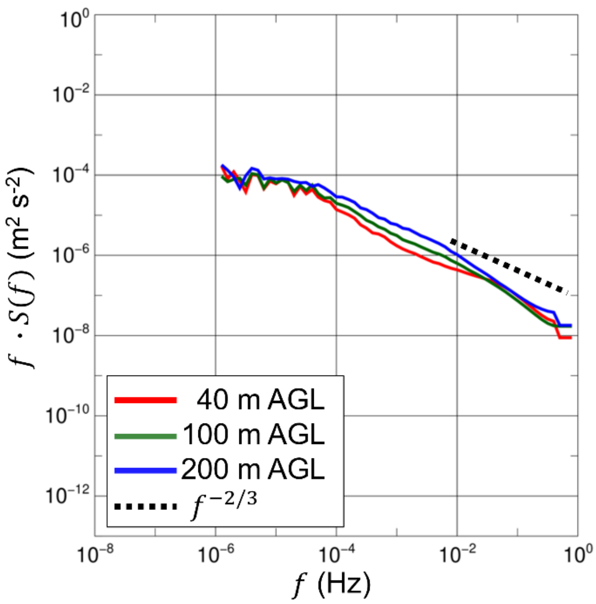

Fig. 6. The binned energy density spectra (*S*) of *w* as a function of frequency (*f*) obtained from the wind lidar at 40 m AGL (red line), 100 m AGL (green line), and 200 m AGL (blue line) over the entire 1-year period of interest. Note that both the x- and y-axes have a logarithmic scale. The black dotted line shows $f^{-2/3}$.

3.2. Wind and Turbulence Characteristics Across All Days

3.2.1. Diurnal Evolution

When averaged across all days within the study period, the mean *WS* was larger during the nighttime than during the daytime for all sampling heights except for the lowest sampling height (i.e., at 40 m AGL) where there was on average a small (~ 0.5 m s^{-1}) increase during the daytime (Fig. 7a, 7b). The daytime decrease in mean WS was largest at the uppermost sampling heights. For example, at 300 m AGL, the mean WS was around 7 m s^{-1} throughout much of the nighttime, but decreased to a minimum of ~ 4 m s^{-1} between 1100 and 1200 LST. The larger WS during the nighttime than during the daytime at the majority of sampling heights is a finding consistent with previous studies at other forested ridgetops located in the eastern U.S. (e.g., Lee et al., 2015). During the nighttime, there is a decoupling between the surface layer and overlying residual layer, whereas during the daytime this difference is reduced due to turbulent mixing within the daytime CBL. Despite the generally larger WS during the nighttime than during the daytime, we note a WS increase between approximately 1000 LST and 1600 LST which is a finding that has been well-documented in flat terrain (e.g., Barthelmie et al., 1996; Zhang and Zheng, 2004; He et al., 2013) and arises due to the downward transport of higher momentum air from aloft caused by vertical mixing within the CBL (e.g., Dai and Deser, 1999). During the nighttime, there is a decoupling between the near-surface winds and winds within the overlying residual layer that results in a larger near-surface vertical gradient in the surface wind speeds that is consistent with previous studies (e.g., He et al., 2013).

The composites of the mean WD revealed that near-surface wind directions were from the northwest during the nighttime but became westerly during the daytime, whereas mean wind directions 300 m AGL were from the west and exhibited little time-of-day dependence (Fig. 7a, 7c). As a result, WD during the nighttime showed considerably more variability with height than WD during the daytime. The vertical WD gradients were smallest between around 1000 LST and 1600 LST. This period, combined with the smallest vertical WS gradients, is indicative of a well-coupled and well-mixed ridgetop CBL. Clearly visible NBL stratification features (i.e., varying WS of 2–8 m s^{-1} across the different sampling heights) were associated with the northerly/northwesterly to southerly/southwesterly shift in wind from the lower to upper heights sampled by the lidar. Furthermore, after the early morning transition period, all the sampling heights exhibited a westerly wind which most likely indicates the dominant impact of gently-varying topography on the wind fields in the lower altitudes. In contrast, the upper sampling heights were relatively remained unaffected by the local topography, which suggests regional flow features over the lidar at its uppermost sampling heights during the nighttime that are aligned with the mean synoptic flow over the region.

Examination of the composites of the mean turbulence characteristics, averaged over the entire study period, revealed that TKE sampled 40 m AGL (300 m AGL) ranged from ~

1.0 m^2 s^{-2} (1.25 m^2 s^{-2}) to 2.5 m^2 s^{-2} (3.0 m^2 s^{-2}) during this same time period (Fig. 7d), whereas σ_w^2 sampled 40 m AGL (300 m AGL) ranged from 0.25 m^2 s^{-2} (0.50 m^2 s^{-2}) during the nighttime to a maximum of 0.75 m^2 s^{-2} (1.25 m^2 s^{-2}) during the early afternoon (Fig. 7e). These findings are characteristic of a well-mixed daytime CBL and stably-stratified NBL. The combined analyses of TKE and σ_w^2 during the entire diurnal cycle reveal a clear pattern yielding their higher values in the upper levels compared to lower levels during both day and night except the early morning transition period. However, the associated vertical gradients were found to be strong during the nighttime than during daytime. Nocturnal gradients could be explained by the flow regimes whereas daytime gradients can be attributed to the CBL surface forcing and associated thermal regimes.

The composites of S were near 0 during the nighttime at all sampling heights and increased during the daytime. The smallest increases occurred at 40 m AGL where daytime values were ~ 0.05 (Fig. 7f). In contrast, the largest increases occurred at the upper sampling heights where daytime values were ~ 0.3 implying a larger proportion of positive vertical velocities than negative vertical velocities, and thus upward transport of TKE and $\overline{w'^2}$, at these sampling heights. Furthermore, the composites of K was larger during the nighttime than during the daytime, with a nighttime maximum of 1 and daytime minimum of 0, respectively, for the majority of the sampling heights (Fig. 7g). This daytime decrease suggests that the distribution of the vertical velocities becomes less peaked and thus less intermittent, and more uniform, during the daytime (e.g., McNicholas and Turner, 2014). The daytime kurtosis decrease is consistent with previous studies that have used wind lidars to sample turbulence characteristics, including the kurtosis evolution, over flat homogeneous terrain as documented by a study by Berg et al. (2017) using observations from the U.S. Department of Energy's Atmospheric Radiation Measurement site in Oklahoma.

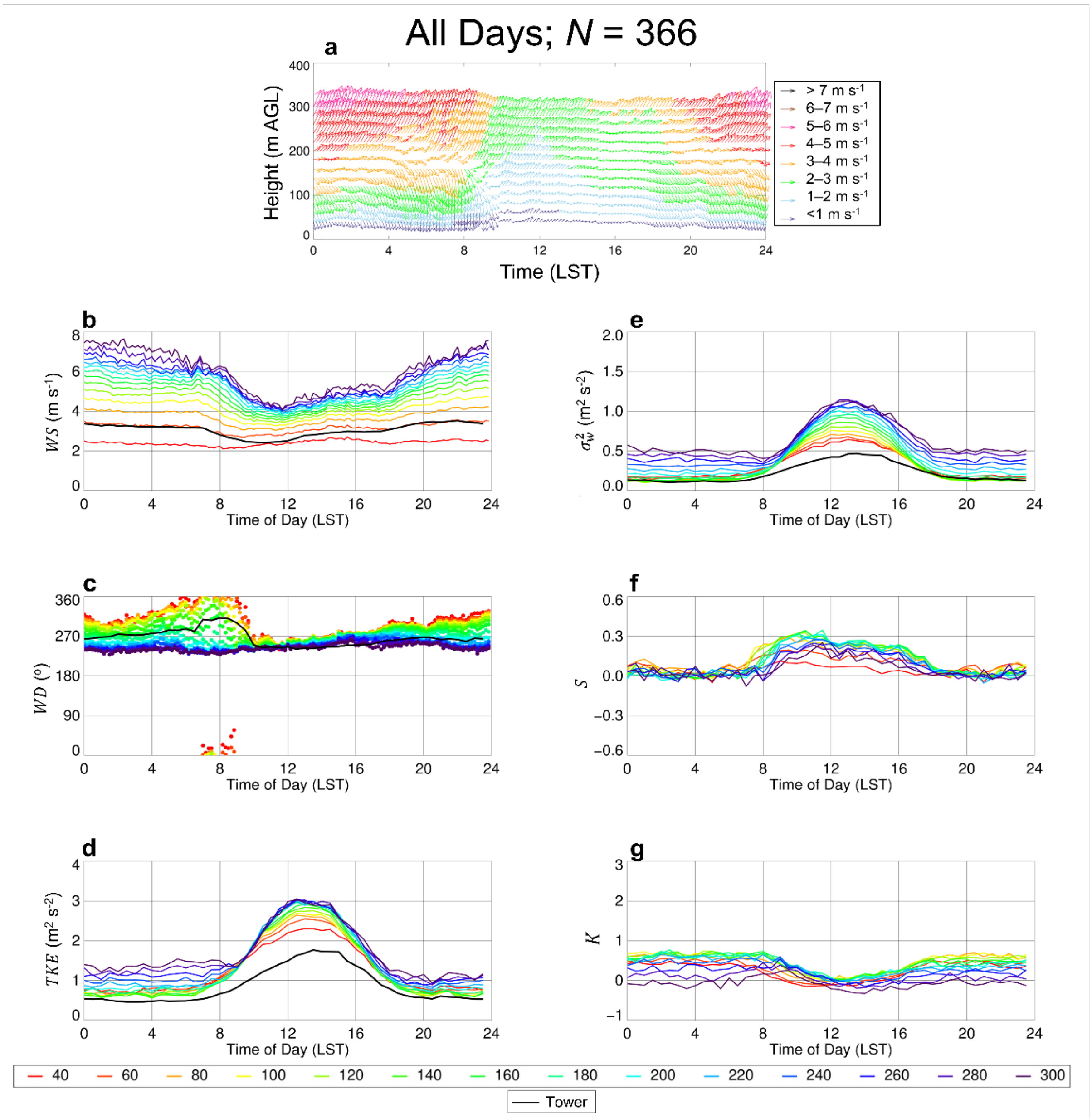

Fig. 7. (a) Wind vectors as a function of time and height, colored by wind speed. (b) The mean diurnal time series of (b) *WS* observed using the wind lidar over the one-year period of interest. Same for (c), (d), (e), (f), and (g), but for *WD*, *TKE*, σ_w^2, *S*, and *K*, respectively. Sampling heights are indicated in the legend at the bottom of the figure. Corresponding values from the micrometeorological tower are shown in panels (b – e), and are indicated with a black line. *N* is shown at the top of the figure.

3.2.2. Seasonal Evolution

When examining the evolution of turbulence characteristics averaged over the entire diurnal cycle (i.e., 0000–2400 LST) on monthly to seasonal timescales, we found that the mean monthly *WS* was larger during the cool season that during the warm season, as mean *WS* at 40 m AGL ranged from a minimum of ~ 2 m s^{-1} in July to ~ 3 m s^{-1} in February (Fig. 8a). Consistent with Fig. 3, the mean monthly *WD* was generally from the west (Fig. 8b).

September and December, however, were the exceptions as we observed mean flows from the northeast during these respective months. We found similar results (not shown) to these when differentiating by time of day.

With larger mean monthly *WS*, the mean monthly *TKE* was also larger during the cool season than during the warm season, ranging from ~ 1 $m^2 s^{-2}$ at 40 m AGL in June through September to ~ 2 $m^2 s^{-2}$ in February (Fig. 8c). Consistent with the seasonal cycle of mean monthly *TKE*, mean monthly σ_w^2 ranged from ~ 0.25 $m^2 s^{-2}$ at 40 m AGL to ~ 0.50 $m^2 s^{-2}$ during this same time period (Fig. 8d). Mean monthly *S* ranged between 0 and 0.2 across all sampling heights and showed little seasonal variability (Fig. 8e), whereas mean monthly *K* was slightly larger during the warm season than during the cool season (Fig. 8f). We also note that, because we are showing the mean values of the turbulence statistics within each month at each sampling height, we are not fully encapsulating the within-month variability in these values which is nontrivial and evident by large standard deviations in the turbulence statistics (not shown) and which may be responsible for the apparent discontinuity in for example the mean monthly σ_w^2 at the uppermost sampling heights (cf. Fig. 8d).

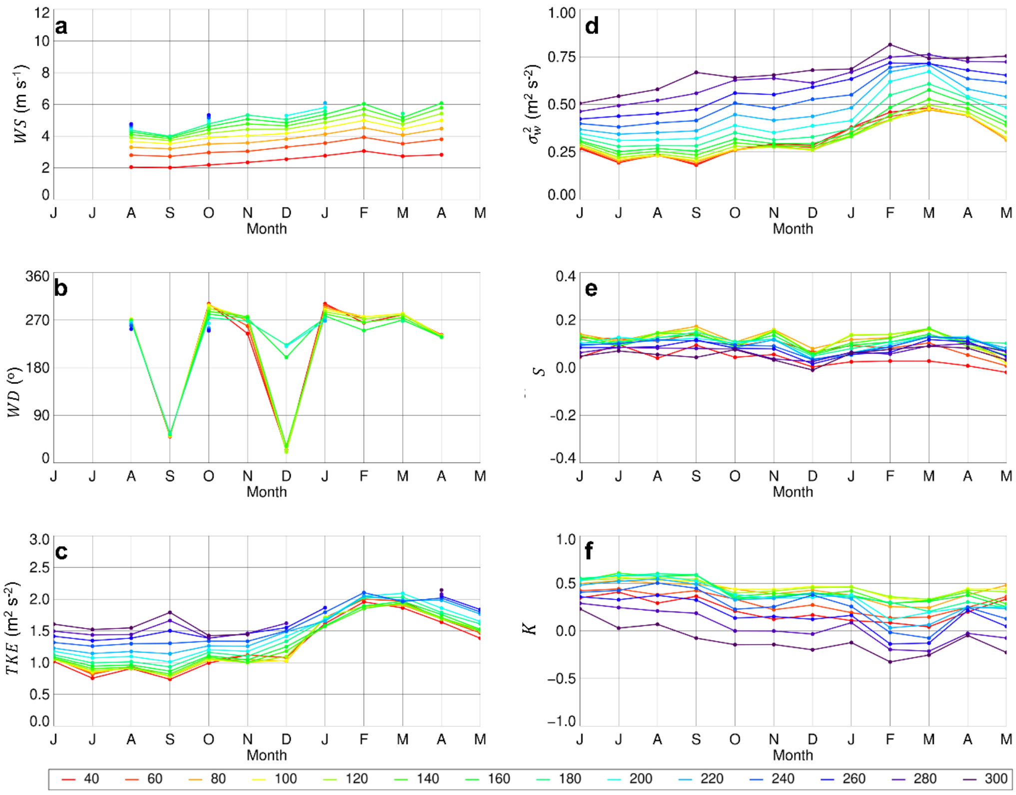

Fig. 8. The mean monthly (a) *WS* observed from the wind lidar over the one-year period of interest and computed between 0000 and 2400 LST. Same for (b), (c), (d), (e), and (f), but for WD, TKE, σ_w^2, S, and K, respectively. Sampling heights are indicated in the legend at the bottom of the figure. Note that only time periods with > 75% valid data (i.e., following the

removal of instances with low CNR, cf. Section 2) are plotted, resulting in periods data which are most apparent in panels (a) and (b).

3.2.3. Relationship between σ_w^2 and TKE

To examine further the turbulence characteristics across all days in the study period, we quantified the relationship between the lidar-derived σ_w^2 and lidar-derived TKE as a function of height above ground level to determine the relative contribution of σ_w^2 to the total TKE at each of the sampling heights. To this end, we computed the Pearson correlation coefficient (r) and the slope of the line of best fit (S) between lidar-derived σ_w^2 and lidar-derived TKE. The Pearson correlation coefficient has been shown to be useful in helping to better understand the evolution of within- and above-canopy turbulence characteristics (e.g., Lee et al., 2025). We found that r was largest nearest the surface and decreased with height. Near-surface r was ~ 0.7 during the middle of the night but ~ 0.9 during the afternoon (Fig. 9a). At the uppermost sampling heights, the diurnal differences were more pronounced, with nighttime r ranging from ~ 0.3–0.5 but daytime values ranging from ~ 0.6–0.8. Furthermore, we found that the slope of the line of best fit between σ_w^2 and TKE as a function of height above ground level was largest between the surface and about 150 m AGL but generally decreased above this height irrespective of time of day (Fig. 9b).

The comparatively large daytime values of r indicate σ_u^2 and σ_v^2 are well correlated with σ_w^2, whereas the smaller values of r indicate that the horizontal wind variances (i.e., σ_u^2 and σ_v^2) have a larger contribution to TKE production at the upper sampling heights during the nighttime. The observed vertical variability in r (i.e., higher value in the lower altitudes than in the upper altitudes) strongly suggest the dominant impact of horizontal (vertical) components of wind field in TKE in the upper (lower) altitudes.

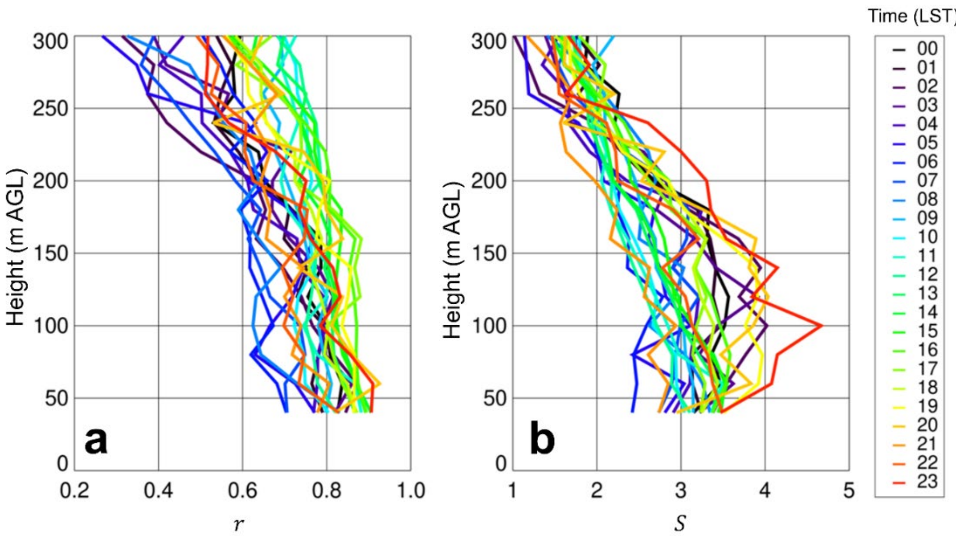

Fig. 9. (a) The Pearson correlation coefficient (i.e., r) and (b) slope of the line of best fit (i.e., S) between σ_w^2 and TKE as a function of height above ground level. Colors indicate the time of day in LST, and are shown to the right of panel (b).

3.3. Turbulence Characteristics under Different Meteorological Conditions During the Daytime

3.3.1. Vertical Velocity Distribution

Discussion so far has focused on the evolution of SL turbulence characteristics irrespective of ambient meteorological regimes. When examining these turbulence characteristics as a function of regime following the procedure outlined in Section 2, we found that the w distributions exhibited positive skewness on the composites of clear days, both for the subsets of days with relatively weak wind speeds and for the subset of days with relatively strong wind speeds across all sampling heights and during both the morning (Table 1) and afternoon (Table 2). These results cumulatively suggest that this is an updraft-dominated turbulence regime when updrafts tend to be narrower and more intense than the broader, weaker downdrafts (i.e., Regimes I and II, shown in Tables 1 and 2, and which have positive S implying strong, narrow updrafts surrounded by weak, extensive downward motion). We also note the percentages of both scenarios ($w > 0$ m s^{-1} and $w < 0$ m s^{-1}) at all three heights across different regimes (see Table 2 and 3). In contrast, the w distributions had negative S on the composites of cloudy days that was likely caused by cloud-top long-wave radiative cooling (e.g., LeMone, 1990; Moeng and Rotunno, 1990; Hogan et al., 2009; Behrendt et al., 2015), including both the subset with weak wind speeds and the subset of days with relatively strong wind speeds. For brevity, we explored the relationship between S and the C_{index} and found a positive relationship between the vertical velocity skewness and

C_{index} at all sampling heights, with the relationship being strongest at 100 m AGL (R^2 = 0.22, S=0.46C_{index}, Fig. 10). These results help us to distinguish bottom up from top down sources of turbulence because vertical transport of $\overline{w'^2}$ by turbulence itself (i.e., w') is reflected within the S values, and S increase as function of C_{index}. Furthermore, we note that K was much larger across all sampling heights during both the morning and the afternoon on the subsets of cloudy days than on the subsets of clear days.

Table 1: The mean ($\overline{w}$), w standard deviation (σ), w skewness (S), w kurtosis (K), percentage $w > 0$ m s^{-1}, and percent of $w < 0$ m s^{-1} between 0800 and 1200 LST. Regime I, II, III, and IV correspond with cases that are clear with weak winds, clear and strong winds, cloudy and weak winds, and cloudy and strong winds, respectively.

Sampling Height	Regime	$\overline{w}$ (m s^{-1})	σ w (m s^{-1})	S	K	% w > 0 m s^{-1}	% w < 0 m s^{-1}
40 m AGL	I	0.11	0.63	0.16	0.45	56.0	44.0
	II	0.07	0.87	0.10	0.53	51.9	48.1
	III	0.04	0.62	-1.12	7.31	50.5	49.5
	IV	-0.11	0.86	-0.59	2.29	46.4	53.6
200 m AGL	I	0.13	0.92	0.55	0.99	51.3	48.7
	II	0.08	1.04	0.53	1.29	49.6	50.4
	III	-0.07	0.67	-1.29	12.32	44.7	55.3
	IV	-0.10	0.85	-0.34	4.15	43.3	56.7
300 m AGL	I	0.13	0.97	0.57	1.30	51.9	48.1
	II	0.08	1.08	0.57	1.70	49.8	50.2
	III	-0.06	0.71	-1.49	15.29	46.5	53.5
	IV	-0.10	0.89	-0.32	4.37	44.1	55.9

Table 2: Same as Table 1, but for times between 1200 and 1600 LST.

Sampling Height	Regime	$\overline{w}$ (m s^{-1})	σ w (m s^{-1})	S	K	% w > 0 m s^{-1}	% w < 0 m s^{-1}
40 m AGL	I	0.06	0.66	0.12	0.38	52.8	47.2
	II	0.05	0.98	0.03	0.44	51.3	48.7
	III	-0.14	0.75	-1.50	7.08	46.7	53.3
	IV	-0.10	0.92	-0.59	2.33	46.9	53.1
200 m AGL	I	0.06	1.04	0.38	0.39	49.0	51.0
	II	0.12	1.24	0.36	0.42	50.6	49.4
	III	-0.16	0.79	-1.57	9.56	40.0	60.0
	IV	-0.13	1.02	-0.55	3.73	43.7	56.3
300 m AGL	I	0.08	1.19	0.37	0.29	49.2	50.8
	II	0.11	1.43	0.44	0.47	49.4	50.6
	III	-0.12	0.78	-1.20	9.71	43.5	56.5
	IV	-0.13	1.10	-0.55	3.63	44.9	55.1

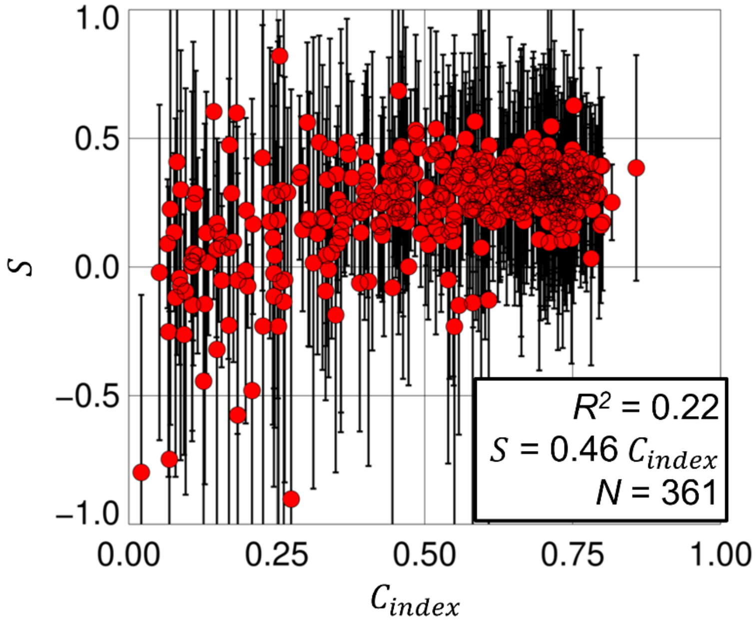

Fig. 10. (a) The relationship between the mean daytime S (red dots; averaged over 0800–1600 LST at 100 m AGL), and the C_{index} obtained from the nearby micrometeorological tower. The error bars represent ± 1 standard deviation in S over the averaging period. The R^2 the best-fit equation, and N are shown in a box on the lower right.

3.3.2. Mean Diurnal Cycles

3.3.2.1. Clear Days

When we examined the mean diurnal cycles of WS observed from the wind lidar on the composite of days in which the C_{index} > 66th percentile and $\overline{WS_{day}}$< 33rd percentile (i.e., clear days with weak wind speeds), we found a small WS decrease during the daytime. The largest values occurred between ~ 0700 and 0800 LST and ranged from 2 m s^{-1} at 40 m AGL to 4 m s^{-1} at 300 m AGL (Fig. 11a, 11b). WD exhibited a clockwise shift during the daytime; between 0700 LST and 1000 LST, winds were easterly at all sampling heights, but between 1000 LST and 1200 LST ranged from southerly to southwesterly (Fig. 11a, 11c). Corresponding with the lower WS during the afternoon, there was greater WD variability at the different sampling heights; near-surface winds were typically southerly, whereas the lidar's uppermost sampling heights winds had a larger southwesterly wind component.

Examination of the evolution of both TKE and σ_w^2 for the composites of clear days with weak wind speeds revealed a broad maximum during the afternoon across all sampling heights. At 40 m AGL (300 m AGL), the maximum values of TKE were ~ 2.0 m^2 s^{-2} (~ 3.5

m^2 s^{-2}) at 40 m AGL (300 m AGL) (Fig. 11d), whereas maximum values of σ_w^2 were ~ 0.5 m^2 s^{-2} (1.5 m^2 s^{-2}) (Fig. 11e). Mean S was typically positive during the daytime for all sampling heights, with maximum values occurring between ~ 0900 and 1100 LST at 140 – 180 m AGL (Fig. 11f) thus indicating the strongest upward transport of TKE and $\overline{w'^2}$ at these sampling heights. Mean K was typically > 0 at all sampling heights between ~ 0700 and 0900 LST but decreased and became < 0 between ~ 1000 LST and 1600 LST (Fig. 11g) which is suggestive of a decrease in turbulence intermittency here that is consistent with the mean diurnal cycles of K that were previously shown.

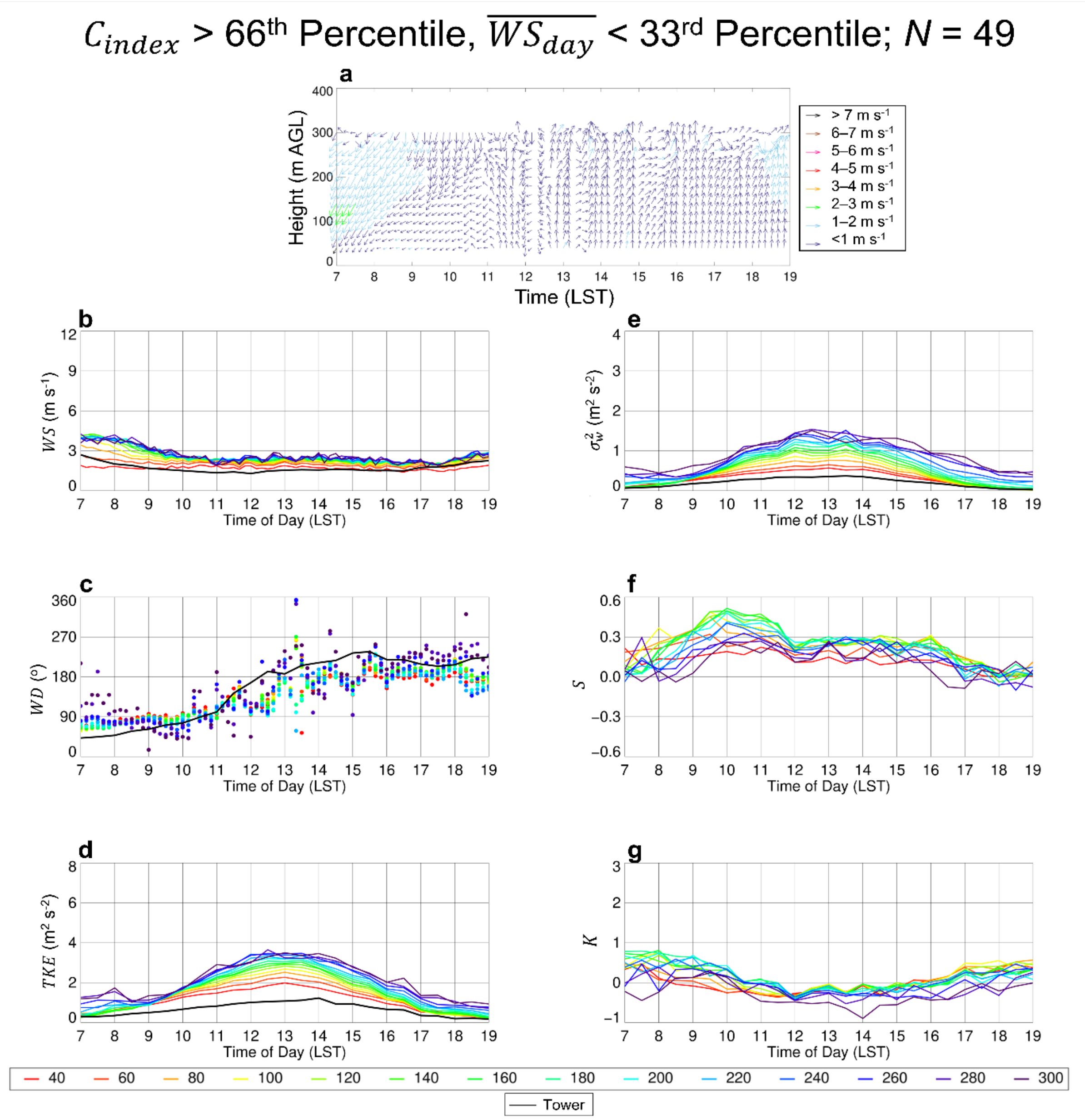

Fig. 11. (a) Wind vectors as a function of time and height, colored by wind speed. (b) The mean diurnal time series, between 0700 LST and 1900 LST, of (a) WS observed from the wind lidar for the composite of days in which the C_{index} > 66th percentile and $\overline{WS_{day}}$ < 33rd percentile (i.e., clear days with weak winds). Same for (c), (d), (e), (f), and (g), but for WD,

TKE, σ_w^2, S, and K, respectively. The sampling heights are indicated in the legend at the bottom of the figure. The corresponding values from the micrometeorological tower are shown in panels (b – e) and are indicated by the black line.

Analogous to the subset of clear days with weak winds, the subset of clear days with strong winds also exhibited a WS decrease during the morning. The minimum WS was observed between ~ 1000 LST and 1100 LST, after which WS increased across all sampling heights (Fig. 12a, 12b). Unlike what was observed in the composites for days with weak winds, there was greater WD variability at all sampling heights between ~ 0700 LST and 0900 LST, with winds backing from the north-northwest at the lowest sampling heights to west-southwest at 300 m AGL (Fig. 12a, 12c) which is opposite to the pattern found on clear days (cf. Fig. 11). This difference disappeared during the mid-morning, and winds showed only minimal backing for the remainder of the day, as west-southwesterly winds were most dominant.

Maximum TKE in the composites for clear days with strong winds ranged from ~ 4 m^2 s^{-2} at 40 m AGL to ~ 6 m^2 s^{-2} at 300 m AGL during the early afternoon (Fig. 12d) due to considerably larger values of σ_u^2 and σ_v^2 on these subsets of days (not shown). However, σ_w^2 was only slightly larger on the composites for clear days with strong winds, as maximum σ_w^2 ranged from ~ 1 m^2 s^{-2} at 40 m AGL to ~ 2 m^2 s^{-2} at 300 m AGL (Fig. 12e). The S and K composites were fairly similar. Accompanying the morning wind direction shift was an increase in S and decrease in K after which these values remained fairly constant throughout the daytime (Fig. 12f, 12g).

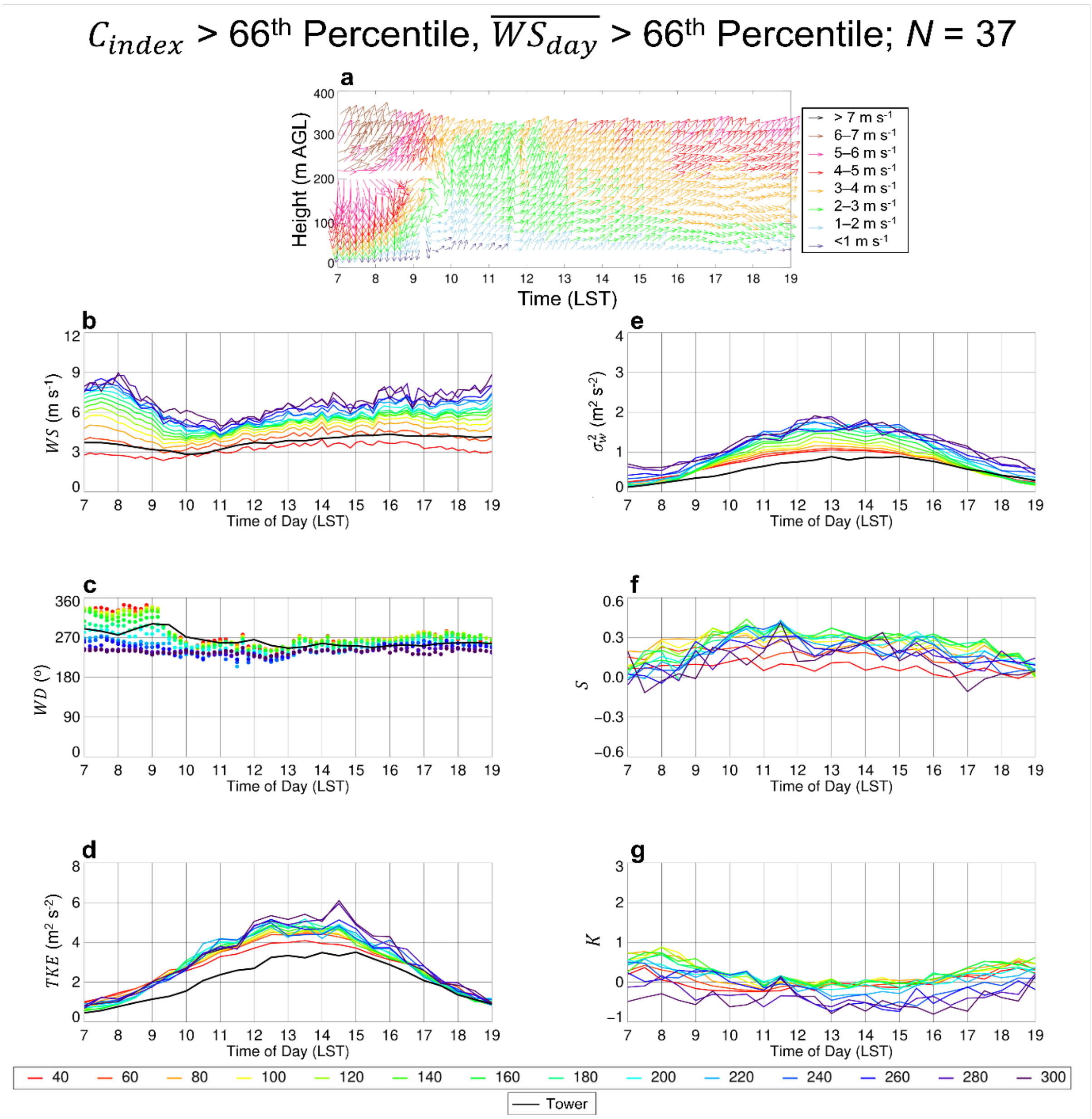

Fig. 12. Same as Fig. 11 but composite for days in which the C_{index} > 66th percentile and $\overline{WS_{day}}$ > 66th percentile (i.e., clear days with strong winds).

3.3.2.2. Cloudy Days

Whereas maximum WS of ~ 4 m s^{-1} at 300 m AGL occurred on cloudy days with weak wind speeds, cloudy days with strong wind speeds had a mean maximum WS of ~ 10 m s^{-1} at 300 m AGL between ~ 1500 and 1700 LST (Fig. 13a, 13b). Similar to the cases with clear skies, however, was that there was a clockwise wind shift during the daytime in the WD composites for cloudy skies and weak winds. Between ~ 0700 LST and 1100 LST, southeasterly winds occurred at all sampling heights (Fig. 13a, 13c). Furthermore, during this period, the winds veered with height, as easterly flows were observed near the surface but southerly flows were observed at 300 m AGL. The composites of WD during the afternoon, however, exhibited little variability with height.

When we examined the turbulence characteristics on the subset of cloudy days and weak wind speeds, we found limited diurnal variability in both TKE (Fig. 13d) and σ_w^2 (Fig. 13e) due to the lack of strong turbulent mixing on this subset of days. Furthermore, vertical gradients in TKE and σ_w^2 were minimal, with maximum values of ~ 0.5 m^2 s^{-2} and 2 m^2 s^{-2}, respectively. Similar to σ_w^2 and TKE, the S composites (Fig. 13f) and K composites (Fig. 13g) showed little diurnal variability and vertical variability; mean values of S (K) were around 0 (0.5) for all sampling heights.

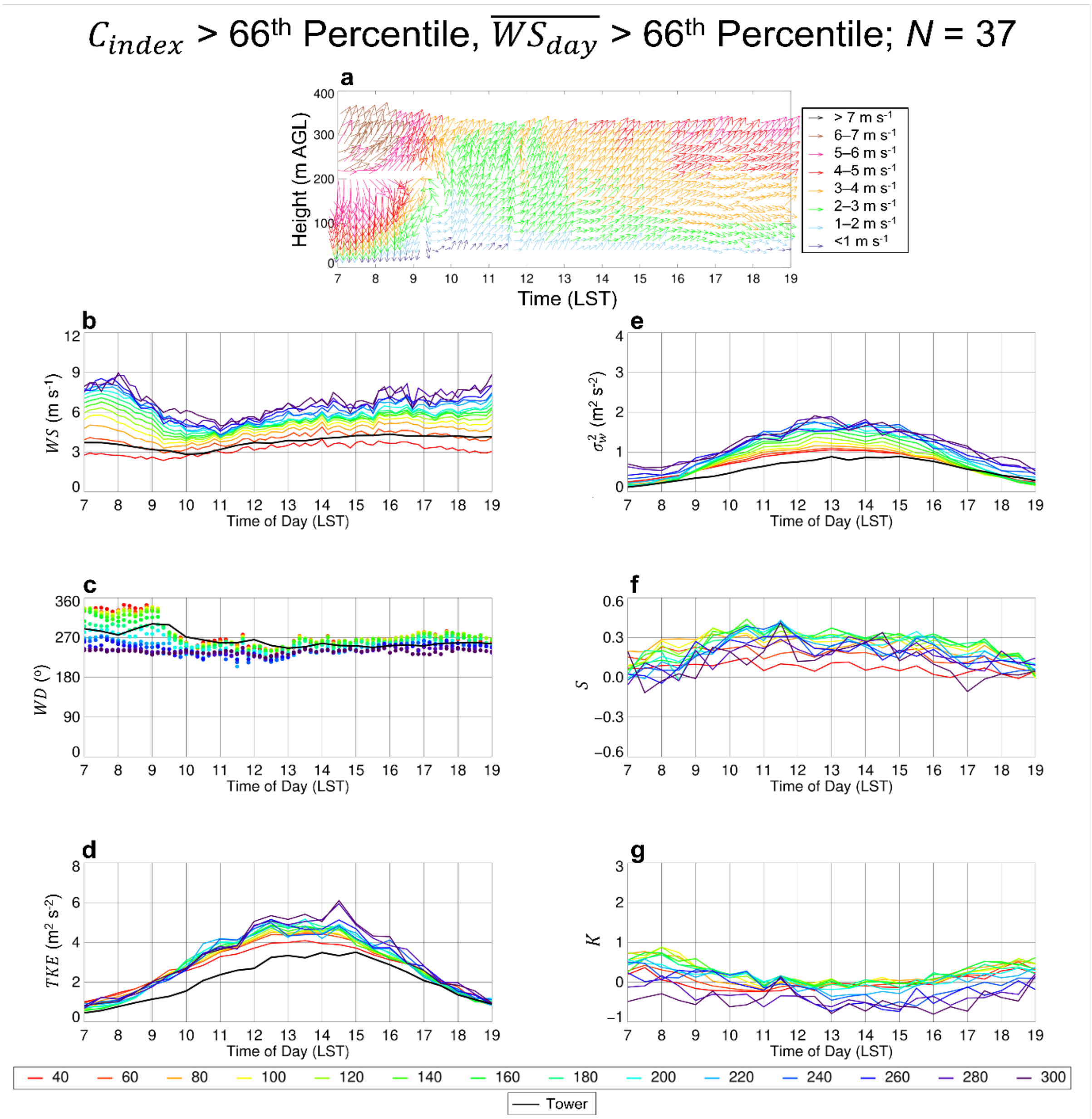

Fig. 13. Same as Fig. 11 but composite for days in which the C_{index} < 33rd percentile and $\overline{WS_{day}}$ < 33rd percentile (i.e., cloudy days with weak winds).

The regimes with the cloudy skies and strong winds had the largest mean WS of any of the four regimes (Fig. 14a, 14b). Near-surface WS were ~ 3 m s^{-1} and exhibited little diurnal variability, whereas mean WS at the uppermost sampling heights were ~ 11 m s^{-1} between 0700 and 0800 LST but decreased to ~ 9 m s^{-1} between 0800 and 1000 LST and showed relatively little variability for the remainder of the day. The WD composite showed westerly winds throughout the diurnal cycle and minimum gradients with height (Fig. 14a, 14c).

The TKE composites showed a small increase during the daytime for the regimes with cloudy skies and strong winds, with values ranging from ~ 2 m^2 s^{-2} post-sunrise to ~ 3 m^2 s^{-2} around noon (Fig. 14d). The σ_w^2 mean diurnal cycles had maximum values between ~ 1200 LST and 1400 LST. During this time period, σ_w^2 ranged from ~ 0.5 m^2 s^{-2} at 40 m AGL to ~ 1.0 m^2 s^{-2} at 300 m AGL (Fig. 14e). Additionally, the σ_w^2 composites exhibited more vertical variability than TKE. The S composites (Fig. 14f) showed a small increase, which was more pronounced at the lidar's uppermost sampling heights than near the surface. Similar to the cloudy regimes with weak wind speeds, the K composites on the subsets of cases with strong winds and cloudy skies showed little diurnal variability, and the mean values were similar among the different sampling heights (Fig. 14g).

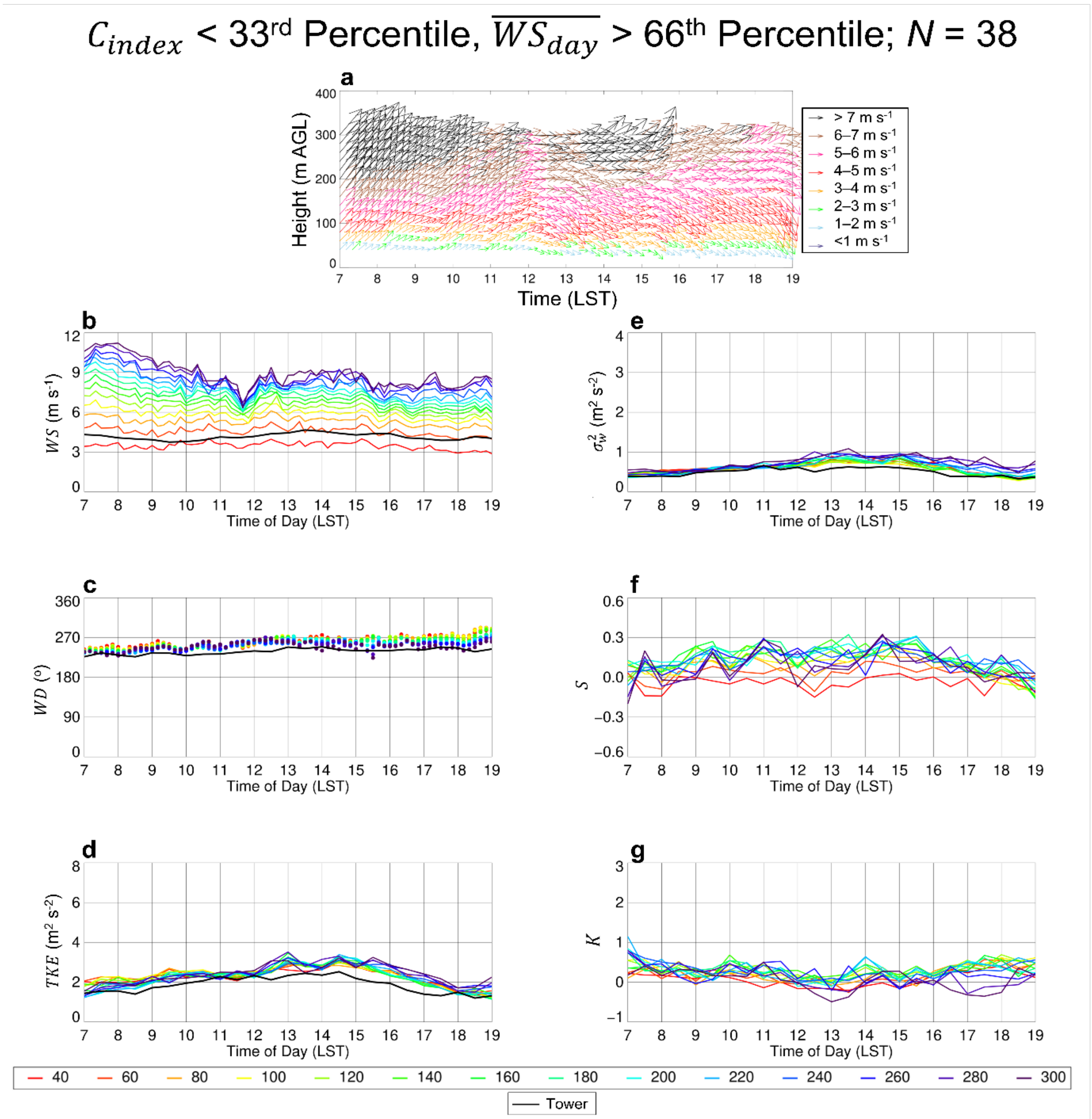

Fig. 14. Same as Fig. 11 but composite for days in which the C_{index} < 33rd percentile and $\overline{WS_{day}}$ > 66th percentile (i.e., cloudy days with strong winds).

3.3.3. Composite Profiles

In the previous section, we examined the diurnal evolution of the near-surface turbulence characteristics under different radiative and wind regimes that we identified during the daytime. We found that $\overline{WS}$ was larger on the subset of cloudy days than on the subset of clear days, possibly due to smoother flows within this subset of cases. The $\overline{WS}$ increased from ~ 4 m s^{-1} at 40 m AGL, both during the morning and afternoon, to ~ 9 m s^{-1} and 8 m s^{-1} during the morning and afternoon, respectively, at 300 m AGL (Fig. 15a). For the majority of the wind and radiative regimes, $\overline{WD}$ was from the west, but there were exceptions (Fig. 15b). During the mornings with cloudy skies and light winds, winds originated from the east below 100 m but veered southward with an increase in height. Winds were also from the east during clear skies and light winds, but these cases exhibited no veering with height. Unlike the other afternoons, wind directions on the subset of days were generally southerly during the afternoon but otherwise the composite mean vertical profiles were quite similar between the morning (0800–1200 LST) and afternoon (1200–1600 LST).

The radiative regime did not affect the $\overline{TKE}$ during the morning, as the profiles on clear days with weak winds were comparable with those on cloudy days with weak winds, with observed values of $\overline{TKE}$ around 1.5 $m^2 s^{-2}$. Mornings with strong winds had $\overline{TKE}$ around 2.5 $m^2 s^{-2}$, irrespective of sky conditions (Fig. 15c). Afternoon profiles had larger variability than the morning. The smallest $\overline{TKE}$ values occurred on cloudy days with weak winds, ranging from 1.5 to 2.0 $m^2 s^{-2}$, whereas $\overline{TKE}$ was oftentimes > 4.0 $m^2 s^{-2}$ on the afternoons with clear skies and strong winds. Examination of $\overline{\sigma_w^2}$ indicated that σ_w^2 was largest on the subsets of clear days, whereby $\overline{\sigma_w^2}$ increased from ~ 0.5 $m^2 s^{-2}$ (~ 1.0 $m^2 s^{-2}$) at 40 m AGL to ~ 1.5 $m^2 s^{-2}$ (~ 2.0 $m^2 s^{-2}$) at 300 m AGL on the subset of days with weak (strong) winds (Fig. 15d). On the remaining subsets of wind and radiative regimes, $\overline{\sigma_w^2}$ remained below 1 $m^2 s^{-2}$ during both the morning and afternoon. $\bar{S}$ exhibited only small differences between the morning and afternoon across all wind and radiative regimes (Fig. 15e).

All regimes had a positive $\bar{S}$ bias that was most positive on the subsets of regimes with clear skies than on cloudy days, whereby the observed $\bar{S}$ was around 0.25 and indicating the strongest upward transport of TKE and $\overline{w'^2}$ (e.g., Hogan et al., 2009) within these turbulent regimes. $\bar{K}$ was positive during the morning across all radiative and wind regime but became negative in the afternoon under clear sky conditions (Fig. 15f). The most negative $\bar{K}$ occurred during the afternoon under regimes with clear skies and weak winds over the lowest 200 m which is suggestive of more turbulence intermittency within this particular meteorological regime (e.g., McNicholas and Turner, 2014).

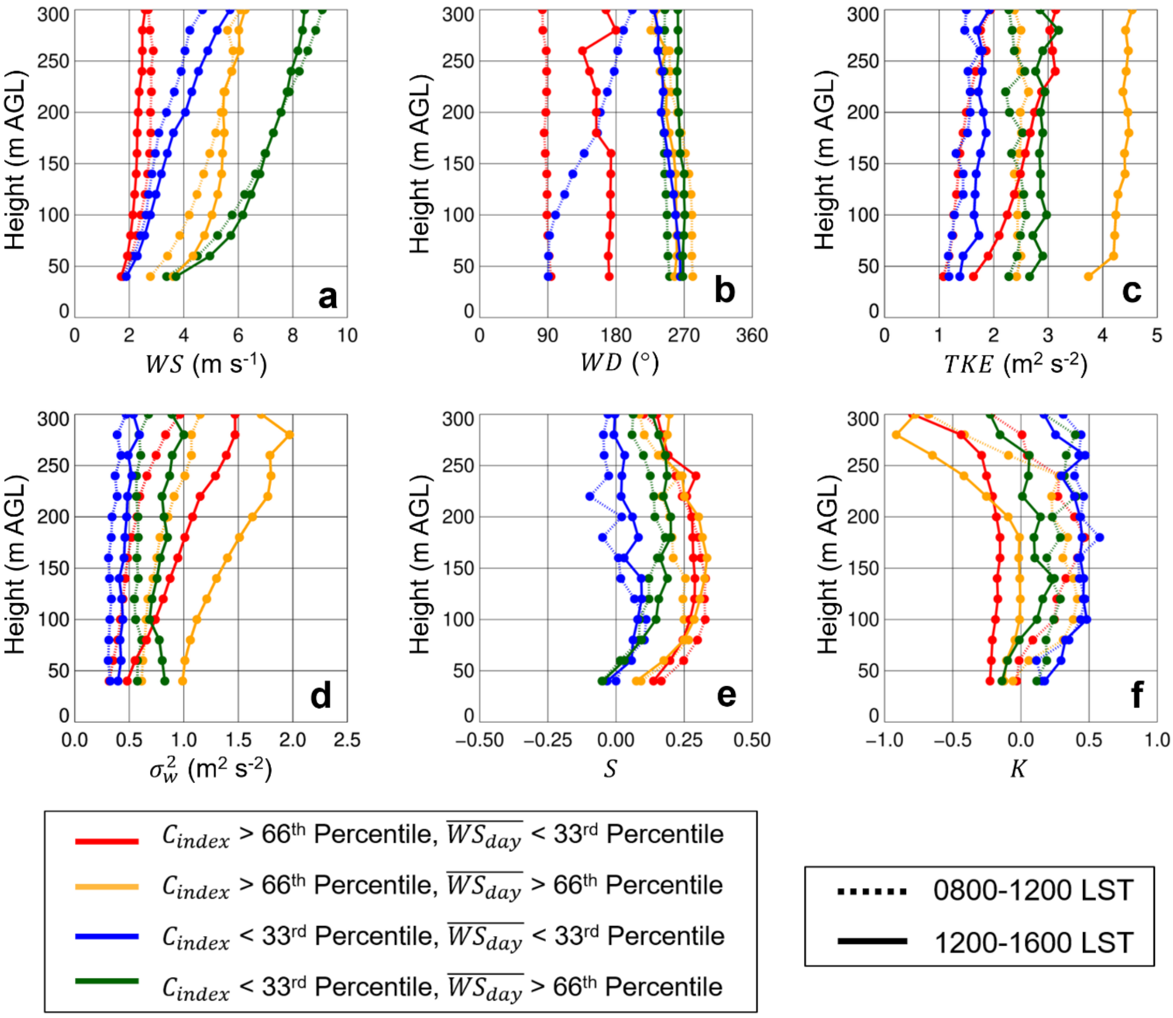

Fig. 15. The mean vertical profiles of (a) WS, (b) WD, (c) TKE, (d) σ_w^2, (e) S, and (f) K during the morning (i.e., 0800–1200 LST, dashed line) and afternoon (i.e., 1200–1600 LST, solid line).

3.4. Turbulence Characteristics under Different Meteorological Conditions During the Nighttime

Discussion has so far focused on the evolution of near-surface turbulence characteristics within the daytime CBL under different radiative and wind regimes but has not yet addressed the turbulence characteristics observed within the NBL. To this end, in the present section, we quantify the near-surface turbulence characteristics under different radiative and wind regimes during the nighttime (i.e., 0000–0400 LST).

3.4.1. Vertical Velocity Distribution

When examining the normalized w distributions from the different sampling heights obtained from the wind lidar under the different radiative and wind regimes during the nighttime, consistent with our findings for daytime conditions, we observed larger skewness on cloudy days than clear days (Table 3). At 40 m AGL, S was -0.08 (0.13) on the subset of clear days with weak winds (strong winds), whereas S was -2.48 (-1.03) on the subset of cloudy days with weak winds (strong winds) resulting in a larger percentage of positive vertical velocities compared to negative vertical velocities. Also consistent with our findings for daytime conditions was that K was larger on the subsets of cases with cloudy skies than on the subsets of cases with clear skies.

Table 3. Same as Table 1 but for times between 0000 and 0400 LST.

Sampling Height	Regime	$\bar{w}$ (m s^{-1})	σ w (m s^{-1})	S	K	% w > 0 m s^{-1}	% w < 0 m s^{-1}
40 m AGL	I	0.05	0.20	-0.08	4.68	63.8	36.2
	II	0.03	0.48	0.13	2.14	52.8	47.2
	III	-0.07	0.56	-2.48	15.45	49.8	50.2
	IV	-0.10	0.72	-1.03	5.33	47.1	52.9
200 m AGL	I	0.01	0.33	-0.07	4.65	52.6	47.4
	II	0.00	0.36	0.11	4.56	49.8	50.2
	III	-0.21	0.73	-3.44	19.09	40.8	59.2
	IV	-0.15	0.69	-1.09	9.57	40.7	59.3
300 m AGL	I	0.02	0.47	0.06	6.99	52.1	47.9
	II	0.01	0.49	-0.09	4.88	52.1	47.9
	III	-0.22	0.80	-3.19	18.79	41.9	58.1
	IV	-0.20	0.74	-1.12	8.22	38.7	61.3

3.4.2. Composite Profiles

$\overline{WS}$ exhibited the largest increase with height in the lowest 100 m of the lidar profile during the nighttime (i.e., 0000–0400 LST). Furthermore, $\overline{WS}$ was largest on nights with clear skies. On these nights, $\overline{WS}$ was > 8 m s^{-1} above ~ 150 m AGL (Fig. 16a). $\overline{WD}$ was typically from the northeast under instances with clear skies and independent of wind speed regime (Fig. 16b). In contrast, instances with cloudy skies were characterized by northwesterly near-surface flows and winds backing to the west with height.

Examination of the $\overline{TKE}$ and $\overline{\sigma_w^2}$ profiles revealed that these quantities were largest under cloudy skies with strong winds, whereby $\overline{TKE}$ and $\overline{\sigma_w^2}$ were 1.5 – 2.0 m^2 s^{-2} and ~ 0.4 m^2 s^{-2}, respectively, throughout the profile (Fig. 16c, Fig. 16d). Conversely, on the subset of clear nights with weak wind speeds, $\overline{\sigma_w^2}$ and $\overline{TKE}$ were < 0.1 m^2 s^{-2} and ~ 0.2 m^2 s^{-2}, respectively, between the surface and ~ 200 m AGL. $\bar{S}$ was slightly positive in the lowest ~ 100 m for all scenarios except for those with clear skies and weak winds. In those scenarios,

$\bar{S}$ was < 0 throughout the profile implying the expected downward transport of $\overline{w'^2}$ and TKE. (Fig. 16e). $\bar{K}$ was ~ 0.5 throughout the profiles and did not exhibit large differences as a function of radiative or wind regime, but was lower at the uppermost sampling heights in all of the scenarios (Fig. 16f), implying a larger degree of turbulence intermittency as a function of height across all of the scenarios.

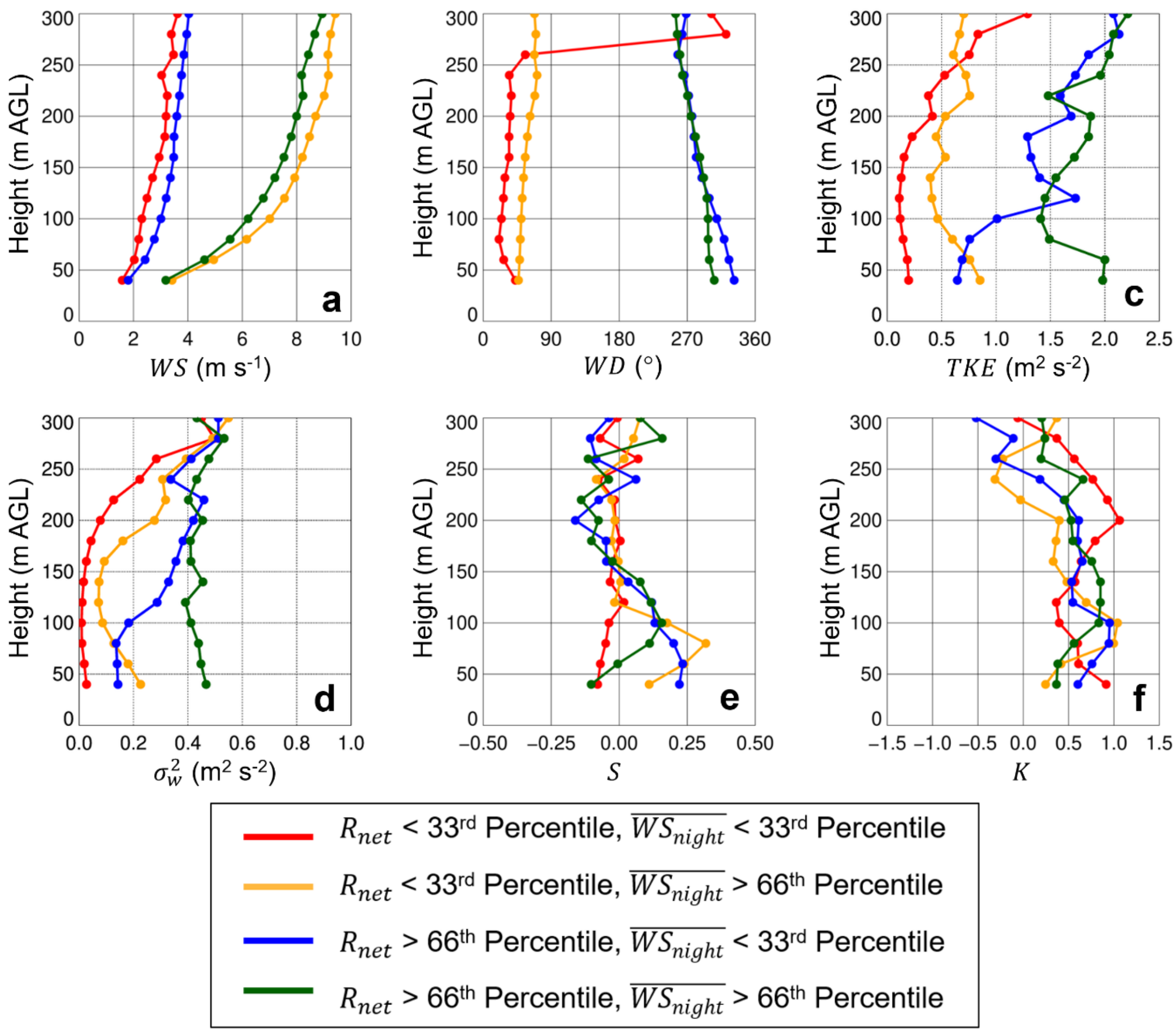

Fig. 16. The mean vertical profiles of (a) WS, (b) WD, (c) TKE, (d) σ_w^2, (e) S, and (f) K during the nighttime (i.e., 0000–0400 LST).

3.5. Turbulence Characteristics as a Function of Wind Direction

To fulfill the fourth objective of this work, we examined the turbulent characteristics as a function of constant wind directions, following the approach enumerated in Section 2.3. Days with constant northeasterly flows, which oriented down the Tennessee Valley (cf. Section 2.1.), exhibited veering winds with height, as northeasterly flows were present in the lowest sampling heights in the observations from the wind lidar, whereas easterly flows were observed at the uppermost sampling heights (Fig. 17). In contrast to the days with constant northeasterly winds, days with constant southwesterly winds, which were those in which the flow was oriented up the Tennessee Valley (cf. Section 2.1.), were characterized by WD exhibited about 25° of backing with height between about 0000 LST and 0900 LST, after which WD was nearly constant with height (Fig. 18).

Whereas WS, TKE, σ_w^2, S, and K exhibited similar characteristics on the composites of days with near-constant northeasterly winds and on the composites of days with near-constant southwesterly winds, the former exhibited greater hour-to-hour variability than the latter. The hour-to-hour variability was particularly evident during the nighttime at the uppermost sampling heights on days with constant northeasterly flows, whereby down-valley drainage flows may induce transient turbulent bursts during these times that result in TKE nearing 2 m^2 s^{-2}. Further investigation of these turbulent bursts will be subject of further study.

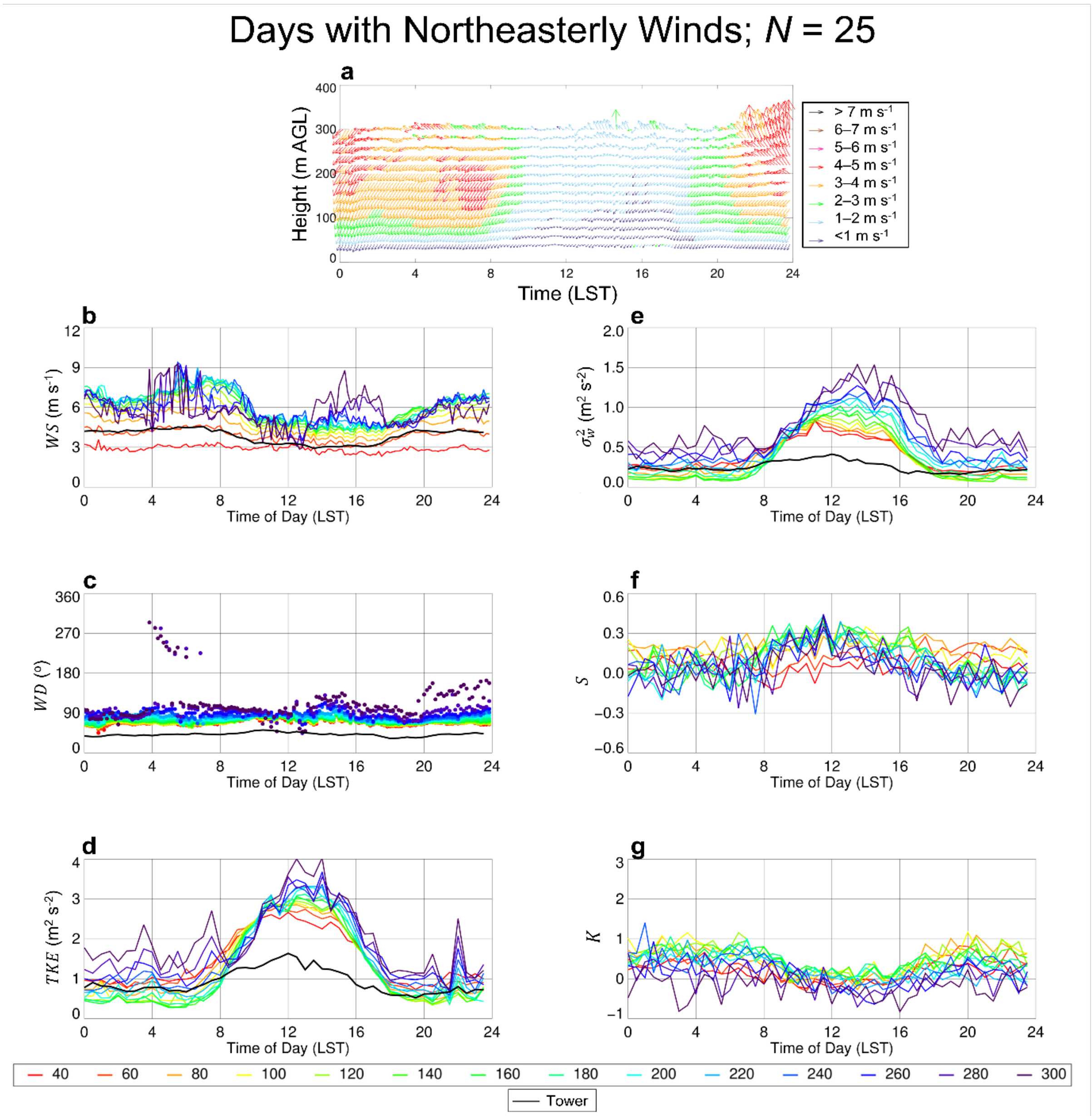

Fig. 17. (a) Wind vectors as a function of time and height, colored by wind speed. (b) The mean diurnal time series of WS observed from the wind lidar for the composite of days with near-constant northeasterly winds. Same for (c), (d), (e), (f), and (g), but for WD, TKE, σ_w^2, S, and K, respectively. The sampling heights are indicated in the legend at the bottom of the figure. The corresponding values from the micrometeorological tower are shown in panels (b – e) and are indicated by the black line.

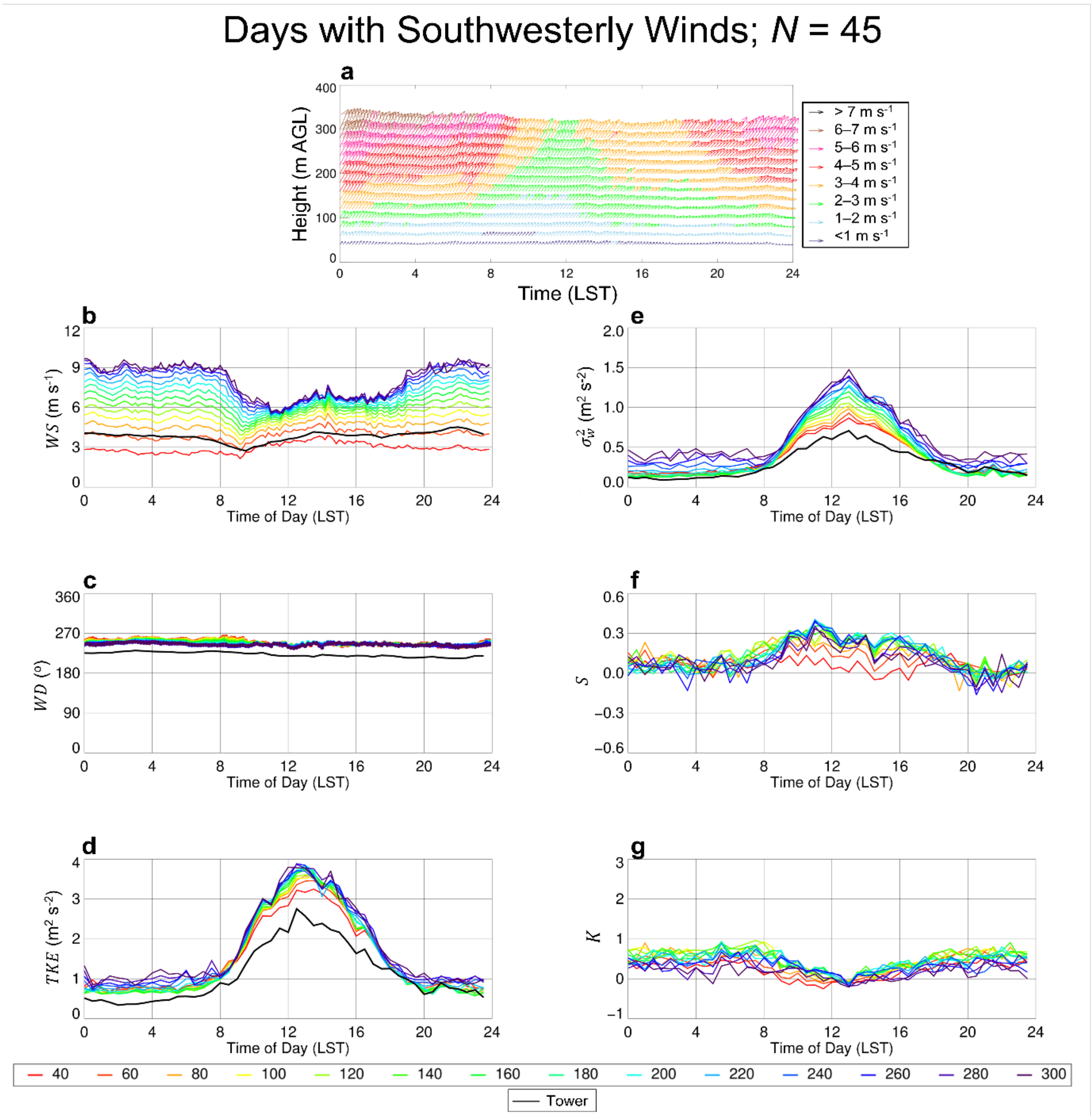

Fig. 18. Same as Fig. 17 but for the composite of days with southwesterly winds.

4. Summary and conclusions

In this study, we addressed the question of how the vertical variability of turbulence characteristics evolves in the lowest few hundred meters of the atmosphere over a deciduous ridgetop forest across different radiative and wind regimes during the daytime convective boundary layer and nocturnal boundary layer. We found that the wind speed, as well as the TKE and σ_w^2, obtained from the lowest sampling height of the wind lidar at ~$1.5h_c$, showed reasonably good agreement with observations obtained from analogous sampling heights at the nearby micrometeorological tower. This finding provided confidence in our choice to use the micrometeorological tower's measurements to study varying meteorological regimes in the study region, in addition to helping provide us with fidelity in the wind speed and, in particular, the turbulence measurements derived from the wind lidar. We quantified the turbulence characteristics within the different radiative and wind regimes by computing the composites of the mean diurnal cycles, $\overline{w}$ frequency distributions, and the mean vertical profiles of the wind and turbulence characteristics. We found that the largest decrease in the diurnal wind speed occurred on clear, windy days. Under clear sky conditions, increasing TKE and σ_w^2 yield positive S throughout the lower part of afternoon ABL. Under cloudy conditions we found a mostly height-independent distribution of TKE which were associated with lower σ_w^2 and near-zero S.

To the best of our knowledge, this study is the first of its kind to document vertical profiles of turbulence statistics, as well as higher-order statistical moments, in the lowest few hundred meters of the atmosphere above a forested ridgetop and how the quantities varied under different forcings: surface heating under clear skies versus cloudy skies whereby the forcing is driven by radiative cooling at the cloud top. The high resolution observations available from the wind lidar used in this study allowed for turbulent characteristics to be examined at higher vertical resolution than has been previously done in other studies using traditional profiling systems. The observations can further be used to provide the boundary conditions for high-resolution NWP models over complex terrain and aid in their evaluation to allow for the refinement of turbulence and SL parameterizations.

Data availability

The observations from the wind lidar and from the micrometeorological tower that were used in this study are available upon request from the corresponding author. The digital elevation model used to aid in the generation of Fig. 1 was obtained from the Parameter-elevation Regressions on Independent Slopes Model (PRISM) climate group at the Northwest Alliance for Computational Science and Engineering and can be accessed from <https://prism.oregonstate.edu/downloads/>.

Acknowledgments

We thank the engineers and technicians from the NOAA Air Resources Laboratory Atmospheric Turbulence and Diffusion Division in Oak Ridge, Tennessee who have helped to maintain wind lidar in addition to the instrumentation along the tower at Chestnut Ridge to ensure high-quality datasets from the lidar and tower. We thank the two anonymous reviewers whose feedback help us strengthen the interpretation of the results presented in this manuscript, as well as the anonymous reviewer from the NOAA Air Resources Laboratory for suggested edits to an earlier version of the manuscript. Lastly, we note that the results and conclusions obtained from this work, as well as any views that we have expressed herein, are those of the authors and may not necessarily reflect those of NOAA or the Department of Commerce.

Appendix A.

As shown in Table A1, the percent of data completion, and of high-quality data, from the wind lidar during the 1-year study period decreased as a function of height. The lowest range gate (i.e., at 40 m AGL) had > 90% completion for TKE, σ_w^2, S, and K. In contrast, the uppermost range gate (i.e., at 300 m AGL) had a data completion of ~ 50% for TKE and ~ 70% for σ_w^2, S, and K.

Table A1. Percent data completion of TKE, σ_w^2, S, and K at each sampling height from the wind lidar during the one-year study period and after filtering periods with CNR < -23 in addition to either missing or physically-unrealistic values.

Height (m AGL)	% Complete TKE	% Complete σ_w^2	% Complete S	% Complete K
40	92.9	95.5	95.6	95.5
60	93.2	95.4	95.4	95.3
80	92.9	95.1	95.1	95.1
100	92.3	94.4	94.5	94.5
120	91.6	93.9	94.0	93.9
140	90.5	93.0	93.2	93.1
160	89.3	92.2	92.3	92.3
180	87.5	91.2	91.4	91.4
200	84.7	90.0	90.3	90.3
220	80.6	88.2	88.5	88.5
240	74.8	85.4	85.9	85.9
260	67.5	81.4	82.0	82.0
280	59.5	76.1	77.0	77.0
300	51.9	69.7	70.7	70.7

Appendix B.

To have confidence that the conclusions from this study were unaffected by our choice of different thresholds, we tested a range of these. When we evaluated the sensitivity of our results to varying C_{index} thresholds under weak winds (i.e., those < 33rd percentile), we found a WS decrease and a clockwise WD change during the daytime that was irrespective of our choice for C_{index} (Fig. A1). There was more scatter present in the mean WD for this subset of cases likely due to a smaller number of cases on days with the C_{index} > 75th percentile. Furthermore, the *TKE* diurnal cycles showed consistency under varying C_{index} thresholds, whereas the maximum daytime values were expectedly when the C_{index} was largest.

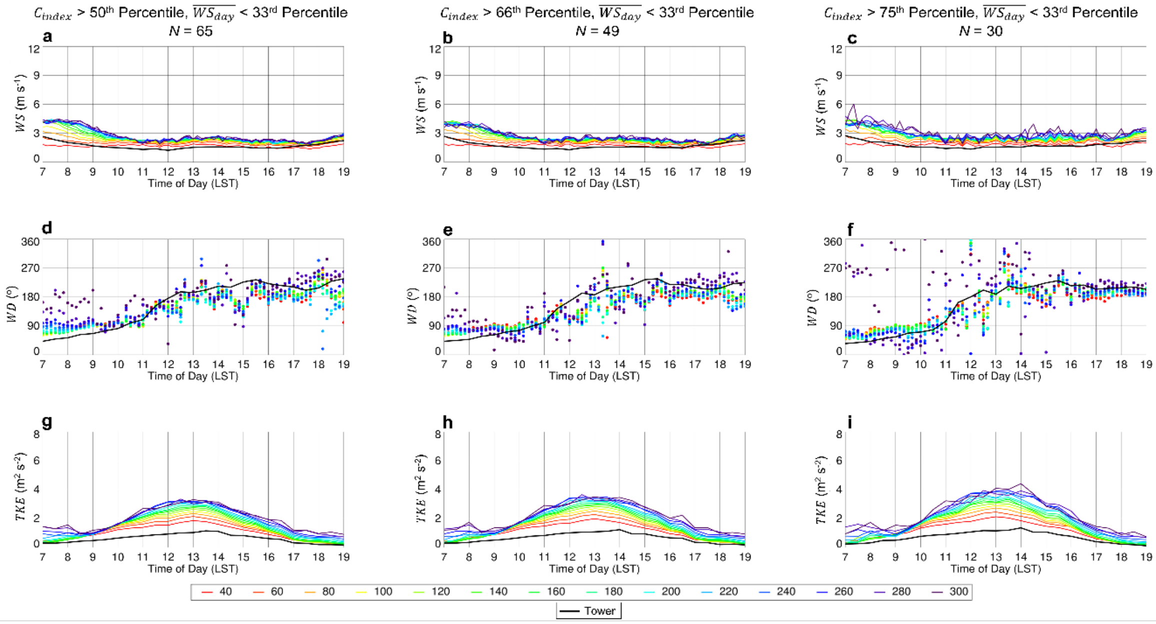

Fig. A1. The mean diurnal time series, between 0700 LST and 1900 LST, of WS observed from the wind lidar for the composite of days in which the $\overline{WS_{day}}$ < 33rd percentile and (a) C_{index} > 50th percentile, (b) > 66th percentile, and (c) > 75th percentile. Same for (d) – (f) and for (g) – (i) but for WD and TKE, respectively. The sampling heights are indicated in the legend at the bottom of the figure. The corresponding values from the micrometeorological tower are indicated by the black line, and the number of cases (*N*) used in the composites is shown at the top of the figure.

References

Adler, B., Gohm, A., Kalthoff, N., Babić, N., Crosmeier, U., Lehner, M., Rotach, M. W., Haid, M., Markmann, P., Gast, E., Tsaknakis, G., & Georgoussis, G. (2021). CROSSINN: A field experiment to study the three-dimensional flow structure in the Inn Valley, Austria. *Bulletin of the American Meteorological Society*, 102, E38–E60. https://doi.org/10.1175/BAMS-D-19-0283.1.

Ansmann, A., Fruntke, J., & Engelmann, R. (2010). Updraft and downdraft characterization with Doppler lidar: cloud-free versus cumuli-topped mixed layer. *Atmospheric Chemistry and Physics*, 10, 7845–7858. https://doi.org/10.5194/acp-10-7845-2010.

Baldocchi, D. D., & Meyers, T. P. (1988a). Turbulence structure in a deciduous forest. *Boundary-Layer Meteorology*, 43, 345–364. https://doi.org/10.1007/BF00121712.

Baldocchi, D. D., & Meyers, T. P. (1988b). A spectral and lag-correlation analysis of turbulence in a deciduous forest canopy. *Boundary-Layer Meteorology*, 45, 31–58. https://doi.org/10.1007/BF00120814.

Baldocchi, D. D., & Meyers, T. P. (1989). The effects of extreme turbulent events on the estimation of aerodynamic variables in a deciduous forest canopy. *Agricultural and forest meteorology*, 48, 117–134. https://doi.org/10.1016/0168-1923(89)90011-7.

Barthelmie, R. J., Grisogono, B., & Pryor. S. C. (1996). Observations and simulations of diurnal cycles of near-surface wind speeds over land and sea. *Journal of Geophysical Research: Atmospheres*, 101, 21327–21337. https://doi.org/10.1029/96JD01520.

Behrendt, A., Wulfmeyer, V., Hammann, E., Muppa, S., & Pal, S. (2015). Profiles of second- to fourth-order moments of turbulent temperature fluctuations in the convective boundary layer: first measurements with rotational Raman lidar. *Atmospheric Chemistry and Physics*, 15, 5485–5500. https://doi.org/10.5194/acp-15-5485-2015.

Berg, L. K., Newsom, R. K., & Turner, D. D. (2017). Year-long vertical velocity statistics derived from Doppler lidar data for the continental convective boundary layer. *Journal of Applied Meteorology and Climatology*, 56, 2441–2454. https://doi.org/10.1175/JAMC-D-16-0359.1

Brugger, P., Träumner, K., & Jung, C. (2016). Evaluation of a procedure to correct spatial averaging in turbulence statistics from a doppler lidar by comparing time series with an ultrasonic anemometer. *Journal of Atmospheric and Oceanic Technology*, 33, 2135–2144. https://doi.org/10.1175/JTECH-D-15-0136.1.

Businger, J. A., Wyngaard, J. C., Izumi, Y., & Bradley, E. F. (1971). Flux-profile relationships in the atmospheric surface layer. *Journal of Atmospheric Science*, 28, 181–189. https://doi.org/10.1175/1520-0469(1971)028<0181:FPRITA>2.0.CO;2.

Dewani, N., Sakradzija, M., Schlemmer, L., Leinweber, R., & Schmidli, J., (2023). Dependency of vertical velocity variance on meteorological conditions in the convective boundary layer. *Atmospheric Chemistry and Physics*, 23, 4045–4058. https://doi.org/10.5194/acp-23-4045-2023.

Dai, A. & Deser, C. (1999). Diurnal and semidiurnal variations in global surface wind and divergence fields. *Journal of Geophysical Research: Atmospheres*, 104, 31109–31125. https://doi.org/10.1029/1999JD900927

De Wekker, S. F. J., & Kossmann, M. (2015). Convective boundary layer heights over mountainous terrain—a review of concepts. *Frontiers in Earth Science*, 3, 77. https://doi.org/10.3389/feart.2015.

Dyer, A. J. (1974). A review of flux-profile relationships. *Boundary-Layer Meteorology,* 7, 363–372. https://doi.org/10.1007/BF00240838.

Fernando, H. J. S., Pardyjak, E. R., Di Sabatino, S., Chow, F. K., De Wekker, S. F. J., Hoch, S. W., Hacker, J., Pace, J. C., Pratt, T., Pu, Z., Steenburgh, W. J., Whiteman, C. D., Wang, Y., Zajic, D., Balsley, B., Dimitrova, R., Emmitt, G. D., Higgins, C. W., Hunt, J. C. R., Knievel, J. C., Lawrence, D., Liu, Y., Nadeau, D. F., Kit, E., Blomquist, B. W., Conry, P., Coppersmith, R. S., Creegan, E., Felton, M., Grachev, A., Gunawardena, N., Hang, C., Hocut, C. M., Huynh, G., Jeglum, M.E., Jensen, D., Kulandaivelu, V., Lehner, M., Leo, L. S., Liberzon, D., Massey, J. D., McEnerney, K., Pal, S., Price, T., Sghiatti, M., Silver, Z., Thompson, M., Zhang, H., Zsedrovits, T. (2015). The MATERHORN: Unravelling the intricacies of mountain weather. *Bulletin of the American Meteorological Society*, 96, 1945–1967. https://doi.org/10.1175/BAMS-D-13-00131.1.

Finnigan, J. F., & Belcher, S. E. (2004). Flow over a hill covered with a plant canopy. *Quarterly Journal of the Royal Meteorological Society*, 130, 1–29. https://doi.org/10.1256/qj.02.177.

Greene, B. R., Kral, S. T., Chilson, P. B., & Reuder, J. (2022). Gradient-based turbulence estimates from multicopter profiles in the Arctic stable boundary layer. *Boundary-Layer Meteorology*, 183, 321–353. https://doi.org/10.1007/s10546-022-00693-x.

Grisogono, B., Sun, J., & Belušić, D. (2020). A note on MOST and HOST for turbulence parametrization. *Quarterly Journal of the Royal Meteorological Society,* 146, 1991–1997. https://doi.org/10.1002/qj.3770.

He, Y., Monahan, A. H., & McFarlane, N.A. (2013). Diurnal variations of land surface wind speed probability distributions under clear-sky and low-cloud conditions. *Geophysical Research Letters*, 40, 3308–3314. https://doi.org/10.1002/grl.50575.

Hogan, R .J., Grant, A. L. M., Illingworth, A. J., Pearson, G. N., & O'Connor, E. J. (2009). Vertical velocity variance and skewness in clear and cloud-topped boundary layers as revealed by Doppler lidar. *Quarterly Journal of the Royal Meteorological Society*, 135, 635–643. https://doi.org/10.1002/qj.413.

Kaimal, J. C., Wyngaard, J. C., Haugen, D. A., Coté, O. R., Izumi, Y., Caughey, S. J., & Readings, C. J. (1976). Turbulence structure in the convective boundary layer. *Journal of the Atmospheric Science*, 33, 2152–2169. https://doi.org/10.1175/1520-0469(1976)033<2152:TSITCB>2.0.CO;2.

Knoop, S., Bosveld, F. C., de Haij, M. J., & Apituley, A. (2021). A 2-year intercomparison of continuous-wave focusing wind lidar and tall mast wind measurements at Cabauw. *Atmospheric Measurement Techniques*, 14, 2219–2235. https://doi.org/10.5194/amt-14-2219-2021.

Kumer, V. M., Reuder, J., Dorninger, M., Zauner, R. & Grubišić, V. (2016). Turbulent kinetic energy estimates from profiling wind LiDAR measurements and their potential for wind energy applications. *Renewable Energy*, 99, 898–910. http://dx.doi.org/10.1016/j.renene.2016.07.014.

Lareau, N. P., Zhang, Y., & Klein, S. A. (2018). Observed Boundary Layer Controls on Shallow Cumulus at the ARM Southern Great Plains Site. *Journal of Atmospheric Science*, 75, 2235–2255. https://doi.org/10.1175/JAS-D-17-0244.1.

Lee, T. R., De Wekker, S. F. J., Andrews, A. E., Kofler, J., & Williams, J. (2012). Carbon dioxide variability during cold front passages and fair weather days at a forested mountaintop site. *Atmospheric Environment*, 46, 405–416. https://doi.org/10.1016/j.atmosenv.2011.09.068.

Lee, T. R., De Wekker, S. F. J., Pal, S., Andrews, A. E., & Kofler, J. (2015). Meteorological controls on the diurnal variability of carbon monoxide mixing ratio at a mountaintop monitoring site in the Appalachian Mountains. *Tellus B: Chemical and Physical Meteorology*, 67, 25659. https://doi.org/10.3402/tellusb.v67.25659.

Lee, T.R., De Wekker, S .F. J., & Pal, S. (2018). The impact of the afternoon planetary boundary-layer height on the diurnal cycle of CO and CO_2 mixing ratios at a low-altitude mountaintop. *Boundary-layer Meteorology*, 168, 81–102. https://doi.org/10.1007/s10546-018-0343-9.

Lee, T. R., Buban, M., Turner, D. D., Meyers, T. P., & Baker, C. B. (2019). Evaluation of the High-Resolution Rapid Refresh (HRRR) model using near-surface meteorological and flux observations from Northern Alabama. *Weather and Forecasting,* 34, 635–663. https://doi.org/10.1175/WAF-D-18-0184.1.

Lee, T. R., & Buban, M. (2020). Evaluation of Monin-Obukhov and bulk Richardson parameterizations for surface-atmosphere exchange. *Journal of Applied Meteorology and Climatolog*y, 59, 1091–1107. https://doi.org/10.1175/JAMC-D-19-0057.1.

Lee, T. R., Buban, M. S., & Meyers, T. P. (2021). Application of bulk Richardson parameterizations of surface fluxes to heterogeneous land surfaces. *Monthly Weather Review*, 149, 3243–3264. https://doi.org/10.1175/MWR-D-21-0047.1.

Lee, T. R., & Meyers, T. P. (2023). New parameterizations of turbulence statistics for the atmospheric surface layer. *Monthly Weather Review*, 151, 85–103. https://doi.org/10.1175/MWR-D-22-0071.1.

Lee, T. R., Leeper, R. D., Wilson, T., Diamond, H., Meyers, T. P., & Turner, D. D. (2023). Using the U.S. Climate Reference Network to identify biases in near- and subsurface meteorological fields in the High-Resolution Rapid Refresh (HRRR) weather prediction model. *Weather and Forecasting*, 38, 879–900. https://doi.org/10.1175/WAF-D-22-0213.1.

Lee, T. R., Pal, S., Krishnan, P., Hirth, B., Heuer, M., Meyers, T. P., Saylor, R. D., & Schroeder, J. (2023). On the efficacy of Monin-Obukhov and bulk Richardson surface-layer parameterizations over drylands. *Journal of Applied Meteorology and Climatology,* 62, 855–875. https://doi.org/10.1175/JAMC-D-23-0092.1.

Lee, T. R., Pal, S., Leeper, R. D., Wilson, T., Diamond, H., Meyers, T. P., & Turner, D. D. (2024). On the importance of regime-specific evaluations for numerical weather prediction models as demonstrated using the High Resolution Rapid Refresh (HRRR) model. *Weather and Forecasting,* 39, 781–791. https://doi.org/10.1175/WAF-D-23-0177.1

Lee, T. R., Pal, S., Krishnan, P., Wilson, T. B., Saylor, R. D., Meyers, T. P., Kochendorfer, J., Pendergrass, W., White, R., & Heuer, M. (2025). Turbulence within and above a deciduous montane forest: The Hockey-Stick Transition Hypothesis (HOST) versus Monin-Obukhov Similarity Theory (MOST). *Agricultural and Forest Meteorology*, 362, 110342. https://doi.org/10.1016/j.agrformet.2024.110342.

Lee, T. R., Pal, S., Meyers, T. P., Krishnan, P., Hirth, Heuer, M., Saylor, R. D., Kochendorfer, J., & Schroeder, J. (2025). The impact of the Bowen ratio on surface layer parameterizations for heat, moisture, and turbulent fluxes over drylands. *Journal of Applied Meteorology and Climatology*. https://doi.org/10.1175/JAMC-D-24-0075.1.

LeMone, M. A. (1990). Some observations of vertical velocity skewness in the convective planetary boundary layer. *Journal of the Atmospheric Sciences*, 47, 1163–1169. https://doi.org/10.1175/1520-0469(1990)047<1163:SOOVVS>2.0.CO;2.

Liao, H., Jing, H., Ma, C., Tao, Q. & Li, Z. (2020). Field measurement study on turbulence field by wind tower and Windcube Lidar in mountain valley. *Journal of Wind Engineering and Industrial Aerodynamics*, 197, 104090. https://doi.org/10.1016/j.jweia.2019.104090.

Maurer V., Kalthoff, N., Wieser A., Kohler, M., Mauder, M., & Gantner, L. (2016). Observed spatiotemporal variability of boundary-layer turbulence over flat, heterogeneous terrain. *Atmospheric Chemistry and Physics*, 16, 1377–1400. https://doi.org/10.5194/acpd-15-18011-2015.

Meyers, T. P. (2016). AmeriFlux BASE US-ChR Chestnut Ridge, Ver. 2-1, AmeriFlux AMP, accessed 21 October 2024.

McNicholas, C., & Turner, D. D. (2014). Characterizing the convective boundary layer turbulence with a High Spectral Resolution Lidar. *Journal of Geophysical Research: Atmospheres*, 119, 12910–12927. https://doi.org/10.5194/10.1002/2014JD021867.

Moeng, C.-H., & R. Rotunno (1990). Vertical-velocity skewness in the buoyancy-driven boundary layer. *Journal of the Atmospheric Sciences*, 47, 1149–1162. https://doi.org/10.1175/1520-0469(1990)047<1149:VVSITB>2.0.CO;2.

Monin, A., & Obukhov, A. (1954). Basic laws of turbulent mixing in the surface layer of the atmosphere. Contributions of the Geophysical Institute Academy of Sciences USSR, 151, e187.

Newman, J. F., Klein, P. M., Wharton, S., Sathe, A., Bonin, T. A., Chilson, P. B., & Muschinski, A. (2016). Evaluation of three lidar scanning strategies for turbulence measurements. *Atmospheric Measurement Techniques*, 9, 1993–2013. https://doi.org/10.5194/amt-9-1993-2016.

Pal, S., Behrendt, A., & Wulfmeyer, V. (2010). Elastic-backscatter-lidar-based characterization of the convective boundary layer and investigation of related statistics. *Annales Geophysicae*, 28, 825–847. https://doi.org/www.ann-geophys.net/28/825/2010/.

Pal, S., & Lee, T .R. (2019). Advected airmass reservoirs in the downwind of mountains and their roles in overrunning boundary layer depths over the Plains. *Geophysical Research Letters*, 46. https://doi.org/10.1029/2019GL083988.

Pal, S., Lee, T. R., Phelps, S., & De Wekker, S. F. J. (2014). Impact of atmospheric boundary layer depth variability and wind reversal on the diurnal variability of aerosol concentration at a valley site. *Science of the Total Environment*, 496, 424–434. https://doi.org/10.1175/JAMC-D-15-0277.1.

Pal, S., De Wekker, S. F. J., & Emmitt, G. D. (2016). Spatial variability of the atmospheric boundary layer heights over a low mountain region: Cases from MATERHORN-2012 field experiment. *Journal of Applied Meteorology and Climatology*, 55, 1927–1952. http://dx.doi.org/10.1175/JAMC-D-15-0277.1.

Patton, E. G., & Katul, G. G. (2009). Turbulent pressure and velocity perturbations induced by gentle hills covered with sparse and dense canopies. *Boundary-Layer Meteorology*, 133, 189–217. http://dx.doi.org/10.1007/s10546-009-9427-x.

Raupach, M. R., & Finnigan, J. J. (1997). The influence of topography on meteorological variables and surface-atmosphere interactions. *Journal of Hydrology*, 190, 182–213. https://doi.org/10.1016/S0022-1694(96)03127-7.

Robey, R., & Lundquist, J. K. (2022). Behavior and mechanisms of Doppler wind lidar error in varying stability regimes. *Atmospheric Measurement Techniques*, 15, 4585–4622. https://doi.org/10.5194/amt-15-4585-2022.

Rotach, M. W., Gohm, A., Lang, M. N., Leukauf, D., Stiperski, I., & Wagner, J. S. (2015). On the vertical exchange of heat, mass, and momentum over complex, mountainous terrain. *Frontiers in Earth Science,* 3, 76. https://doi.org/10.3389/feart.2015.

Salesky, S. T., & Chamecki, M. (2012). Random errors in turbulence measurements in the atmospheric surface layer: Implications for Monin–Obukhov similarity theory. *Journal of Atmospheric Science*, 69, 3700–3714. https://doi.org/10.1175/JAS-D-12-096.1.

Sathe, A., & Mann, J. (2013). A review of turbulence measurements using ground-based wind lidars. *Atmospheric Measurement Techniques*, 6, 3147–3167. https://doi.org/10.5194/amt-6-3147-2013.

Sorbjan, Z., & Grachev, A. A. (2010). An evaluation of the flux–gradient relationship in the stable boundary layer. *Boundary-Layer Meteorology,* 135, 385–405. 10.1007/s10546-010-9482-3.

Strauch, R. G., Merritt, D. A., Moran, K. P., Earnshaw, K. B., & Van de Kamp, D. (1984). The Colorado wind-profiling network. *Journal of Atmospheric and Oceanic Technology*, 1, 37–49. https://doi.org/10.1175/1520-0426(1984)001<0037:TCWPN>2.0.CO;2.

Stiperski, I., & Rotach, M. W. (2016). On the measurement of turbulence over complex mountainous terrain. *Boundary-Layer Meteorology*, 159, 97–121. https://doi.org/10.1007/s10546-015-0103-z.

Sun J., Mahrt, L., Banta, R. M., Pichugina, Y. L. (2012). Turbulence regimes and turbulence intermittency in the stable boundary layer during CASES-99. *Journal of Atmospheric Science*, 69, 338–351. https://doi.org/10.1175/JAS-D-11-082.1.

Sun, J., Takle, E. S., & Acevedo, O. C. (2020). Understanding physical processes represented by the Monin-Obukhov bulk formula for momentum transfer. *Boundary-Layer Meteorology*, 177, 69–95. https://doi.org/10.1007/s10546-020-00546-5.

Van de Wiel, B. J. H., Moene, A. F., Jonker, H. J. J., Baas, P., Basu, S., Donda, J. M. M., Sun, J., & Holtslag, A. A. M. (2012). The minimum wind speed for sustainable turbulence in the nocturnal boundary layer. *Journal of Atmospheric Science*, 69, 3116–3127. https://doi.org/10.1175/JAS-D-12-0107.1.

Wagner, T. J., Turner, D. D., Heus, T., & Blumberg, W. G. (2022). Observing profiles of derived kinematic field quantities using a network of profiling sites. *Journal of Atmospheric and Oceanic Technology*, 39, 335-351. https://doi.org/10.1175/JTECH-D-21-0061.1.

Webb, E. K., Pearman, G. I., & Leuning, R. (1980). Correction of flux measurements for density effects due to heat and water vapour transfer. *Quarterly Journal of the Royal Meteorological Society*, 106, 85–100. https://doi.org/10.1002/qj.49710644707.

Wharton, S., Ma, S., Baldocchi, D. D., Falk, M., Newman, J. F., Osuna, J. L., & Bible, K. (2017). Influence of regional nighttime atmospheric regimes on canopy turbulence and gradients at a closed and open forest in mountain-valley terrain. *Agricultural and Forest Meteorology*, 237, 18–29. http://dx.doi.org/10.1016/j.agrformet.2017.01.020.

Whiteman, C. D., & Allwine, K. J. (1986). Extraterrestrial solar radiation on inclined surfaces. *Environmental Software*, 1, 164–169. https://doi.org/10.1016/0266-9838(86)90020-1.

Whiteman, C. D., Bian, X., & Zhong, S. (1999). Wintertime evolution of the temperature inversion in the Colorado Plateau Basin. *Journal of Applied Meteorology and Climatology*, 38, 1103–1117. https://doi.org/10.1175/1520-0450(1999)038<1103:WEOTTI>2.0.CO;2.

Whiteman, C. D. (2000). Mountain Meteorology: Fundamentals and Applications. Oxford University Press, 355 pp.

Wilson, T. B., & Meyers, T. P. (2007). Determining vegetation indices from solar and photosynthetically active radiation fluxes. *Agricultural and Forest Meteorology*, 144, 160–179. https://doi.org/10.1016/j.agrformet.2007.04.001.

Wilson, T. B., Meyers, T. P., Kochendorfer, J., Anderson, M. C., & Heuer, M. (2012). The effect of soil surface litter residue on energy and carbon fluxes in a deciduous forest. *Agricultural and Forest Meteorology,* 61, 134–147. https://doi.org/10.1016/j.agrformet.2012.03.013.

Wilson, T. B., Kochendorfer, J., Meyers, T. P., Heuer, M., Sloop, K., & Miller J. (2014). Leaf litter water content and soil surface CO2 fluxes in a deciduous forest. *Agricultural and Forest Meteorology*, 192–193, 42–50. https://doi.org/10.1016/j.agrformet.2014.02.005.

Wulfmeyer, V., Behrendt, A., Kottmeier, C., Corsmeier, U., Barthlott, C., Craig, G. C., Hagen, M. Althausen, D., Aoshima, F., Arpagaus, M., Bauer, H.-S., Bennett, L., Blyth, A., Brandau, C., Champollion, C., Crewell, S., Dick, G., Di Girolamo, P., Dorninger, M., Dufournet, Y., Eigenmann, R., Engelmann, R., Flamant, C., Foken, T., Gorgas, T., Grzeschik, M., Handwerker, J., Hauck, C., Höller, H., Junkermann, W., Kalthoff, N., Kiemle, C., Klink, S., König, M., Krauss, L., Long, C. N., Madonna, F., Mobbs, S., Neininger, B., Pal, S., Peters, G., Pigeon, G., Richard, E., Rotach, M. W., Russchenberg, H., Schwitalla, T., Smith, V., Steinacker, R., Trentmann, J., Turner, D. D., van Baelen, J., Vogt, S., Volkert, H., Weckwerth, Wernli, H., Wieser, A., & Wirth, M. (2011). The Convective and Orographically-induced Precipitation Study (COPS): the scientific strategy, the field phase, and research highlights. *Quarterly Journal of the Royal Meteorological Society*, 137, 3–30. https://doi.org/10.1002/qj.752.

Zhang, D. L., & Zheng, W. Z. (2004). Diurnal cycles of surface winds and temperatures as simulated by five boundary layer parameterizations. *Journal of Applied Meteorology*, 43, 157–169. https://doi.org/10.1175/1520-0450(2004)043<0157:DCOSWA>2.0.CO;2.